Virtues of the Visible; Voluminous Vistas & Velocities

by

Jonathan Carrick

A thesis
presented to the University of Waterloo
in fulfillment of the
thesis requirement for the degree of
Master of Science
in
Physics

Waterloo, Ontario, Canada, 2014

© Jonathan Carrick 2014

Author's Declaration

I hereby declare that I am the sole author of this thesis. This is a true copy of the thesis, including any required final revisions, as accepted by my examiners.

I understand that my thesis may be made electronically available to the public.

Abstract

Peculiar velocities are the motions of objects in excess of that resulting from the expansion of the Universe. They arise from gravitational interactions, and as such, probe the underlying distribution of dark matter on large scales. Early work in this field was in part driven to explain the peculiar motion of the Local Group of galaxies (LG) inferred from the dipole in the cosmic microwave background to be 627 ± 22 km s^{-1} towards $l = 276^\circ \pm 3^\circ$, $b = 30^\circ \pm 2^\circ$. Recent work has yet to fully account for this observed motion, with the literature suggesting structures beyond 150 h^{-1}Mpc may have considerable contributions. Furthermore, several studies have recently claimed a large volume about the LG is participating in bulk flow, suggesting the existence of coherent structure on larger scales then predicted by the current cosmological paradigm. In this work we attempt to address these issues: how is matter distributed in the local Universe, what structures source the motion of the Local Group, and is there evidence of a bulk flow in excess of predictions from ΛCDM?

Using redshifts from the 2M++ redshift compilation, we reconstruct the density of galaxies within 200 h^{-1}Mpc, allowing for the first time good sampling of important superclusters such as the Shapley Concentration. In this work we compare the predicted velocities from 2M++ to Tully-Fisher and Type Ia Supernova peculiar velocity measurements. We measure a value of $\beta^* \equiv \Omega_{\rm m}^{0.55}/b^* = 0.431 \pm 0.021$, and $\sigma_{8,{\rm g}} = 0.99 \pm 0.04$, suggesting $\Omega_{\rm m}^{0.55}\sigma_{8,{\rm lin}} = 0.401 \pm 0.024$. This value of $\Omega_{\rm m}^{0.55}\sigma_{8,{\rm lin}}$ is found to be in strong agreement with measurements from independent methods (including recent analyses of CMB temperature anisotropies). The acceleration of the Local Group arising from 2M++ alone is found to be 540 ± 40 km s^{-1}, towards $l = 268^\circ \pm 4^\circ$, $b = 38^\circ \pm 6^\circ$, only 10° out of alignment with the CMB dipole, the best agreement found to date. To account for velocity contributions arising from objects beyond the 2M++ volume, we fit simultaneously for β^* and an external dipole in our analysis. We find that such an external velocity model is preferred at the 5.1σ level, with the best fit velocity being 159 ± 23 km s^{-1} towards $l = 304^\circ \pm 11^\circ$, $b = 6^\circ \pm 13^\circ$. Finally, we measure the predicted bulk flow of a 50 h^{-1}Mpc Gaussian-weighted volume centred on the Local Group. The bulk flow is found to be 230 ± 30 km s^{-1} in the direction $l = 293^\circ \pm 8^\circ$, $b = 14^\circ \pm 10^\circ$, in good agreement with predictions from ΛCDM.

Acknowledgements

I would like to thank my family for all the support and encouragement they have provided over the past years. I am also indebted to Guilhem Lavaux for the invaluable insights and contributions he provided over the course of this degree. Finally, this work would not have been possible without the patient guidance and supervision provided by Mike Hudson.

Table of Contents

List of Tables

List of Figures

Chapter 1

Introduction

Cosmology is the natural science that strives to answer the most fundamental of questions: how did all that we observe come to exist, what physical laws govern this existence, and what is the eventual fate of the Universe? It is a discipline driven by observation, in which discoveries have the potential to alter fundamental perspectives. Over the past century, developments in this field have led us to re-evaluate the significance of our role in the cosmos.

Arguments in favour of the existence of dark matter are extensive and date back to the early 20$^{\text{th}}$ century (Zwicky, 1933; Oort, 1940; Ostriker et al., 1974; Einasto et al., 1974). It was later argued from the upper limits on the temperature anisotropies of the cosmic microwave background (CMB) that the Universe is likely even dominated by non-baryonic dark matter (Bond & Efstathiou, 1984). Furthermore, through analysis of galaxy clustering on large scales, Maddox et al. (1990) found observations suggest that the total matter content of the Universe was substantially less than previously assumed. In order to rectify low matter density with the successes of a Universe of critical energy density, Efstathiou et al. (1990b) proposed re-introduction of the cosmological constant, *i.e.* that empty space is endowed with non-zero energy-density, comprising as much as $\sim$80% of the energy content of the Universe.

As a positive vacuum energy-density would result in accelerating expansion of the Universe, measuring the rate of change in the expansion could in principle lead to detection of a cosmological constant. Using an empirical relationship between the peak luminosities of Supernovae Ia and their light curves, two groups (Riess et al., 1998; Perlmutter et al., 1999) found that the Universe was in fact undergoing *accelerated* expansion. These findings have since been confirmed through careful analysis of CMB temperature fluctuations (de Bernardis et al., 2000), and the results seem conclusive: baryons and light comprise a meagre 5% of the energy content of the Universe, with dark matter comprising 23%, and dark energy constituting 72%. To date, the nature of 95% of the energy content in the Universe remains largely unknown.

The properties of dark matter and dark energy can only be inferred indirectly through their influence on baryons and light. Aside from analysis of the CMB and supernovae, other methods have recently been employed in an attempt to measure dark energy. For instance, Afshordi et al. (2004) and others have made a tentative detection of the Integrated-Sachs Wolfe effect, the net gravitational redshift of a photon as it passes through a potential well that changes over time as a result of positive vacuum energy. Such a detection would be a smoking gun for the existence of dark energy.

As dark matter and dark energy comprise 95% of the content in Universe, their role in moulding the rich structures we observe today cannot be understated. It is commonly believed that these structures formed in the crucible of deep gravitational wells. And as dark matter accounts for a large majority of the mass content in the Universe, a better understanding of dark matter is central to understanding the formation and observed properties of galaxies, galaxy clusters, superclusters and voids.

Deviations from the motion induced by the expansion of the Universe arise through gravitational interactions, and are referred to as peculiar velocities (PVs). As the majority of the matter content in the Universe is dark in nature, peculiar velocities probe the underlying distribution of dark matter, and are in fact the only means of doing so on large scales in the low redshift Universe. As measured PVs can be used to constrain the amplitude of mass fluctuations on a range of scales, and as the amplitude of such fluctuations are cosmology dependent, the analysis of peculiar velocities provides a direct means of constraining cosmology. In this work we attempt to map the underlying distribution of dark matter by constraining the relationship between the distribution of dark matter and the local distribution of galaxies from the 2M++ redshift catalogue (Lavaux & Hudson, 2011). We do so by comparing predicted PVs derived from this density field to measured peculiar velocities from the First Amendment compilation of nearby supernovae (Turnbull et al., 2012), and SFI++ (Springob et al., 2007), a Tully-Fisher sample.

Before delving in to methodology and results, we first discuss theoretical underpinnings and model assumptions of this work. In §1.1 we briefly review historical developments in the field of cosmology. In §1.2 we outline key results derived from the gravitational instability paradigm; specifically, the relation between peculiar velocities and matter density. In §1.3 we motivate the concept of linear biasing. In §1.4 we review the relationship between observed redshifts, peculiar velocities and cosmology. We review procedures used in measuring distances to extragalactic sources in §1.5, and outline methods used in constraining cosmological parameters with peculiar velocities in §1.6. We conclude this chapter by providing a structural overview of this work. Unless stated otherwise, theory derived in these sections draw primarily from Mo et al. (2011).

1.1 Background

In the early 20$^{\text{th}}$ century, while analyzing spectrograms from spiral nebulae Slipher (1917) found that a large majority of his sample (21 of 25) had their spectrum shifted towards larger wavelengths. He accounted for the observed redshifts as arising from a Doppler shift due to the bulk motion of the nebulae. In turn, he estimated that the Milky Way too had a velocity with respect to the nebulae of $\sim$700 km s^{-1}. His findings strongly suggested that there was outward trend in the motion of the objects which comprise the Universe. This work was published at a time when belief in a static Universe was commonplace. In fact, in the same year Einstein (1917) was introducing the cosmological constant Λ in to his field equations to impose such a static Universe. Slipher's measurements, however, would eventually be instrumental in dealing the conclusive blow to the static cosmological model.

It was discovered by Leavitt (1908) that an empirical relationship exists between the periodicity in brightness of Type I Cepheid stars with their intrinsic luminosity. In combination with the measured flux, this relation can be used to determine the star's distance. Famously, while at the Mount Wilson Observatory Hubble used Cepheid distance measurements in combination with the observed redshifts of Slipher to find that extragalactic nebulae are receding from us with radial velocities proportional to their measured distances (Hubble 1929). Subscribing to the Copernican principle that we do not hold a preferred location in the Universe, the same trend in recessional velocities should be observed at all other locations in space. The Hubble relation thus implies that the Universe is expanding. The implications of such a conclusion are paramount. If the Universe is expanding, it follows that it was smaller, more dense and likely hotter in the past. Furthermore, Gamow (1946) showed that had the Universe originated from an initial state of high density (10^{10} g/cm^3) and temperature (10^{10} K) and thereafter undergone rapid expansion and cooling, the observed abundance of elements in the Universe could naturally be explained as resulting from thermonuclear reactions at early times. A natural repercussion of this "Hot Big Bang" model would be the prevalence of residual heat in the form of background thermal radiation peaked in the microwave.

Since its detection (Penzias & Wilson, 1965), analysis of the cosmic microwave background (CMB) has been instrumental in shaping the standard cosmological paradigm. When the Universe was in its infancy it was hot, dense and highly ionized. At this time photons were frequently scattered by ionized particles. As a result, upon expansion and cooling of the Universe the spectrum produced by these interactions was that of a black body, which today corresponds to 3 degrees Kelvin. Shortly after its discovery, using a 8GHz differential radiometer Conklin (1969) detected the CMB temperature was peaked at 13$^{\text{h}}$ right ascension while observing 32°declination. Constraints on the amplitude and direction of this peak have tightened considerably over the years (for a historical review see Lineweaver 1997), and what has since been measured as a dipole is commonly understood to be due to a Doppler shift arising from the motion of the Earth with respect to the rest frame of the CMB. Upon accounting for the Earth's motion around the Sun, the motion of the Sun with respect to the Milky Way, and the motion of the Milky Way with respect

to the gravitationally bound local group of galaxies (LG), there is a residual ∼600 km s^{-1} which has yet to be fully accounted for (see §1.6.2 for further discussion). This fact aside, when working in the rest frame of the CMB one of the most striking characteristics of the temperature distribution is its high level of isotropy, with deviations from the mean temperature being ∼0.001% (Kogut et al., 1993). Analysis of the CMB has thus reinforced the notion that the Universe was largely homogeneous and isotropic at early times.

1.2 Linear Perturbation Theory

The standard cosmological paradigm subscribes to the *cosmological principle*, *i.e.* the belief that the Universe is both homogeneous and isotropic on large scales. In the framework of General Relativity (GR) such a Universe is well described by the Friedmann-Lemaître-Robertson-Walker (FLRW) metric. This metric incorporates an isotropic time-dependence in its spatial components, $g^{ii} = a(t)$ $(i = 1, 2, 3)$, known as the scale factor which allows for rescaling of physical distances with time. Using this metric, from the Einstein field equations we obtain the Friedmann equation

$$H^2 \equiv \left(\frac{\dot{a}}{a}\right)^2 = \frac{8\pi G}{3}\sum_i \epsilon_i - \frac{kc^2}{a^2 R_0^2}, \tag{1.1}$$

where H is the Hubble parameter or expansion rate, G is Newton's gravitational constant, ϵ is the matter-energy density components of the Universe, R_0 is a constant with dimensions of length, and where k describes the geometry of the Universe (+1 for a closed 3-sphere, 0 for flat or Euclidean, and −1 for an open 3-hyperboloid). The scale factor describes the size of the Universe relative to the present, t_0, where we set $a(t_0) = 1$. As Equation (1.1) dictates the time evolution of the scale factor, it is apparent that the the total energy content has important implications for the overall space-time geometry of the Universe. Furthermore, the rate of expansion or collapse is here shown to depend on the relative and overall energy density of the components in the Universe. As previously discussed, such a dynamic Universe is well motivated by observations, which likewise suggest a ΛCDM standard cosmological model comprised of leptons, photons, baryons, a cosmological constant, and cold dark matter.

The rich structures we observe today were initially seeded by small density fluctuations which grew through gravitational instability. As a result, the dynamics of such a process are well described in the framework of linear perturbation theory. In considering a Universe which is initially isotropic, homogeneous, and subject to expansion, we can encapsulate the laws which govern the evolution of matter density, ρ, by writing the equations for mass continuity, force, and gravitation *i.e.*

$$\frac{\partial \rho}{\partial t} + \nabla \cdot (\rho \mathbf{V}) = 0, \tag{1.2}$$

$$\frac{\partial \mathbf{V}}{\partial t} + (\mathbf{V} \cdot \nabla)\mathbf{V} + \nabla\phi = 0, \tag{1.3}$$

$$\nabla^2\phi - 4\pi G\rho \ = 0, \tag{1.4}$$

where $\mathbf{V}$ is the velocity, ϕ is the gravitational potential, G is the gravitational constant, and where derivatives are with respect to proper coordinates, d. We have neglected pressure in Equation (1.3) as this term is assumed to be negligible. We the define the density contrast, δ, as

$$\delta(\mathbf{R}, t) \equiv \frac{\rho(\mathbf{R}, t) - \bar{\rho}}{\bar{\rho}}, \tag{1.5}$$

where $\bar{\rho}$ is the mean density of the Universe. Upon switching to comoving coordinates, $R \equiv d(t)/a(t)$, where $d(t)$ is the proper distance, and where a is the scale factor and encapsulates the expansion of the Universe, we can expand Equations (1.2-1.4) to first order in all quantities. Upon combination of the resulting first order perturbation equations we obtain the following result:

$$\frac{\partial^2\delta}{\partial t^2} + \frac{2\dot{a}}{a}\frac{\partial\delta}{\partial t} = 4\pi G\bar{\rho}\delta. \tag{1.6}$$

The solution to Equation (1.6) involves one mode which decays with time, and one which grows: $D(t)$. As at late times the growing mode dominates, we obtain the key result

$$\nabla \cdot \mathbf{v} = -a\frac{\dot{D}}{D}\delta = -a\frac{dD}{D}\frac{\dot{a}}{da}\delta = -a\frac{dD}{D}\frac{a}{da}\frac{\dot{a}}{a}\delta = -afH\delta, \tag{1.7}$$

where $\mathbf{v}$ is the comoving velocity, *i.e.* the deviation from the Hubble flow, H is the Hubble parameter given by $H(t) = \dot{a}(t)/a(t)$, and where $f \equiv \frac{d\ln D}{d\ln a}$ is known as the growth factor and is a function of the matter density of the Universe. Specifically, the growth factor is a function of the ratio of the matter density of the Universe to the critical density, $\Omega_{\rm m} \equiv \rho/\rho_{\rm c}$, where $\rho_{\rm c} \equiv 3H^2/3\pi G$. For future convenience we define the comoving distance in km s^{-1}, r, through $r \equiv HR$. Equation (1.7) can then be inverted to yield the key result

$$\mathbf{v}(\mathbf{r}) = \frac{af(\Omega_{\rm m})}{4\pi}\int d^3\mathbf{r}'\frac{\delta(\mathbf{r}')(\mathbf{r}' - \mathbf{r})}{(\mathbf{r}' - \mathbf{r})^3}, \tag{1.8}$$

i.e. peculiar velocities are proportional to gravitational accelerations. In order to make use of this relation, however, one must first adopt a biasing scheme which maps the density contrast of galaxies (which can be obtained from a redshift catalogue), to the density contrast of matter.

1.3 Biasing

The concept of biasing was first introduced by Kaiser (1984) when studying the clustering of Abell clusters. It was argued that if clusters formed in regions where the primordial density contrast of galaxies is large, then the correlation function of clusters are a biased measure of the correlation function of galaxies. Specifically, he found that $\xi_{\rm clusters} \approx b^2 \xi_{\rm g}$, where

$$\xi(\mathbf{r}) \equiv \langle \delta(\mathbf{x}) \delta(\mathbf{x}+\mathbf{r}) \rangle \tag{1.9}$$

is the two-point correlation function, b is the biasing parameter, and where subscript "g" is used when referring to galaxies. The two-point correlation function is a measure of the probability in excess of a Poisson distribution of observing an object within a distance r of another object. For an isotropic and homogeneous Universe, Equation (1.9) can be written $\xi(r) \equiv \langle \delta(x) \delta(|\mathbf{x}+\mathbf{r}|) \rangle$. The same argument has since been extended to relate the distribution of galaxies with respect to the underlying distribution of matter (Bardeen et al. 1986), *i.e.*

$$\xi_{\rm g} \approx b^2 \xi_{\rm m}. \tag{1.10}$$

In practice, however, the following relation is generally assumed:

$$\delta_{\rm g} = b \delta_{\rm m}, \tag{1.11}$$

which together with Equation (1.9) implies Equation (1.10), although the converse is not true.

When such a linear mapping is assumed we can in turn obtain a relationship between the mean mass fluctuations of galaxies in a spherical window to those of matter. We define the root mean square mass fluctuations in a spherical window of radius R, $\sigma_{\rm R}$, as

$$\sigma_{\rm R}^2 \equiv \langle \delta^2 \rangle_{\rm R} = \left\langle \left(\int d^3\mathbf{r} W_{\rm R}(|\mathbf{r}-\mathbf{x}|) \delta(\mathbf{r}) \right)^2 \right\rangle, \tag{1.12}$$

where $W_{\rm R}(|\mathbf{r}-\mathbf{x}|)$ is 1 for $\mathrm{R} \geq |\mathbf{r}-\mathbf{x}|$, and 0 otherwise. In combination with Equation (1.11), Equation (1.12) implies

$$\sigma_{\rm g,R} = b \sigma_{\rm m,R}. \tag{1.13}$$

The relation encapsulated by Equations (1.11) and (1.13) is commonly referred to as *linear biasing*. This relation is not formally correct (*cf.* $b > 1$ permits $\delta < -1$), and furthermore assumes a deterministic mapping between mass and luminosity. Analysis of

N-body simulations, however, have found this relation to be in reasonable agreement with simulation results (Dekel & Lahav 1999). With the exception of Appendix B, linear biasing will therefore be assumed throughout the bulk of this work.

1.4 Redshift-Distance Relation

As we will be working in comoving coordinates, we must account for cosmological effects which may introduce systematic bias in extracting distances and velocities from observed redshifts. In this section we briefly review the theoretical underpinnings of these relations.

A galaxy's redshift is defined as:

$$z_{\rm obs} \equiv \frac{\lambda_{\rm obs} - \lambda_{\rm emit}}{\lambda_{\rm emit}} \;\Rightarrow\; 1 + z_{\rm obs} = \frac{\lambda_{\rm obs}}{\lambda_{\rm emit}}, \tag{1.14}$$

where $\lambda_{\rm emit}$ and $\lambda_{\rm obs}$ are the emitted and observed wavelengths, respectively. As a galaxy's redshift results from peculiar motion of that galaxy and in turn the expansion of the Universe, the resulting observed redshift is given by

$$(1 + z_{\rm obs}) = (1 + z_{\rm cos})(1 + z_{\rm pec}), \tag{1.15}$$

where $z_{\rm cos}$ is the cosmological redshift, and where $z_{\rm pec}$ is that resulting from radial peculiar motion. An object's peculiar redshift results from gravitational interactions. For a galaxy with radial peculiar velocity, $v_{\rm pec}$, its resulting peculiar redshift is given by

$$z_{\rm pec} = \sqrt{\frac{1 + v_{\rm pec}/c}{1 - v_{\rm pec}/c}} - 1 \;\approx\; v_{\rm pec}/c, \tag{1.16}$$

where c is the speed of light, and where the approximation is valid for $v_{\rm pec} \ll c$. An object with no peculiar motion, however, will have an observed redshift equal to its cosmological redshift, given by

$$1 + z_{\rm cos} = \frac{a(t_0)}{a(t_{\rm emit})}. \tag{1.17}$$

By Taylor expanding the scale factor about the present, t_0, using Equation (1.17) one can write the lookback time $(t_0 - t)$ as a function of redshift. This relation can in turn be used to relate the cosmological redshift to the proper distance at low redshifts, yielding

$$H_0 R \approx c \left[z_{\rm cos} - \frac{(1 + q_0)}{2} z_{\rm cos}^2 \right]. \tag{1.18}$$

where R is the comoving distance, and q_0 is the deceleration parameter given by

$$q_0 = -\frac{\ddot{a}_0 a_0}{\dot{a}_0^2} = \frac{\Omega_{\rm m}}{2} - \Omega_\Lambda \tag{1.19}$$

for a Universe in which pressure is negligible.

Thus, in order to extract the peculiar velocity from an observed redshift, one first computes $z_{\rm cos}$ from the comoving distance using Equation (1.18), and in turn obtains $v_{\rm pec} \approx c z_{\rm pec}$ from $z_{\rm cos}$ and $z_{\rm obs}$ using Equation (1.15). In determining the peculiar velocity, therefore, an independent measurement of the distance to a galaxy is required in combination with an observed redshift. The following section summarizes some of the more common methods employed in obtaining such measured distances.

1.5 Distance Measurements

All acquired knowledge on astronomical objects is derived from careful analysis of the radiation that they either emit or absorb. Conclusions must therefore be drawn based on the flux within a specified frequency range as measured on Earth. If the intrinsic luminosity of an object could be determined, one could then use the measured flux to infer the object's distance. In combination with observed redshifts, these distances could in turn be used to extract comoving coordinates and velocities.

Very few distance measurements are direct, that is, many of the methods require assumptions about the nature of the object being observed. For objects within a few kpc, however, distances can be obtained from trigonometric parallax, *i.e.* through measuring the observed displacement of nearby stars with respect to more distant background stars at different positions in the Earth's orbit. Indirect methods typically involve use of an assumed empirical or theoretical relationship relating the absolute magnitude of an object to an observable trait. The luminosity derived from such a relationship can then be used in combination with the measured flux to determine the object's distance. These quantities are related through

$$F = \frac{L}{4\pi d_{\rm L}^2}, \tag{1.20}$$

where L is the intrinsic luminosity, F is the observed flux integrated over all frequencies, and where $d_{\rm L}$ is the luminosity distance, and is related to the comoving distance through $d_{\rm L} = (1 + z_{\rm cos})R$. Type I Cepheids, for instance, are a class of pulsating star which alternate between a large, more luminous state, and a smaller, dimmer state. As previously mentioned, there is a tight empirical relationship for these stars between their luminosity and observed period of pulsation, a relationship which can be exploited to obtain their absolute magnitudes (for a recent review see Barnes 2009). In general, indirect methods

require calibration, and each method is calibrated off of those which work at successively closer distances. As such, distance measurement methods form a *cosmic distance ladder*, of which the direct measurement of trigonometric parallax forms the bottom rung.

There are a variety of distance measurement methods used today, however, an exhaustive review of these is beyond the scope of this thesis. Here we will briefly outline those methods which are relevant to the data employed in this work. For a comprehensive discussion on the determination of distances in astronomy see Freedman & Madore (2010).

1.5.1 Type Ia Supernovae

Type Ia Supernovae occur in binary star systems in which a white dwarf accretes matter from its companion (typically another white dwarf). It is believed that ignition results once enough mass has been accumulated ($\sim$1.38 $M_\odot$), increasing core pressure and temperature to sufficient levels to induce carbon fusion. Once fusion is initiated, a runaway reaction is instigated resulting in a cataclysmic nuclear explosion releasing sufficient energy to unbind the star and outshine the host galaxy (Whelan & Iben, 1973).

The resulting emission from these supernovae (SNe) are observed to follow a characteristic light curve, *i.e.* obey a trend in the relative luminosity as a function of time. Furthermore, the peak luminosity of SNe Ia were found to be tightly correlated with their light curve (Phillips, 1993). Once the absolute zero-point of this relation is calibrated externally, *e.g.* using Cepheids (Riess et al., 2009), these SNe become valuable tools enabling distance measurements with a precision of $\sim$10%.

1.5.2 Tully-Fisher Relation

The Tully-Fisher (TF) relation is an empirical relationship first reported by Tully & Fisher (1977) relating the intrinsic luminosity of a spiral galaxy (corrected to face-on inclination to account for extinction) to the maximum velocity of its rotation curve (corrected to edge-on inclination). This relationship is most clearly expressed as

$$L = AV_{\rm max}^{\alpha}, \tag{1.21}$$

where A and α are constants to be determined through calibration. Although the TF parameters can be calibrated externally, *e.g.* using Cepheids (Tully & Pierce, 2000), unlike most distance measurement methods external calibration is not necessary. When deep surveys are used the parameters A and α can be obtained by using spirals from within one cluster, or by assuming the mean peculiar motion of distant galaxy clusters are at rest and using a subset of galaxies from each to calibrate the relation (Masters et al., 2006). Values for the parameter α are found to be wavelength-dependent (Sakai et al., 2000). Values typically range from $\sim$3-4, with scatter in the relation also being wavelength-dependent

and limiting the precision of derived distances to ∼15-20% (Giovanelli et al., 1997; Sakai et al., 2000; Tully & Pierce, 2000).

1.6 Constraining Cosmology With Velocities

Here we build on the groundwork laid in the previous sections and outline how constraints on cosmological parameters can in practice be obtained using peculiar velocities. We then review historical results employing these methods, and thereafter review the current state of the field. We conclude by discussing our approach in resolving open questions, and then outline the structure of this thesis.

1.6.1 Key Results From Theory

Under the assumption of linear biasing, we can re-write Equation (1.8) as

$$\mathbf{v}(\mathbf{r}) = \beta \int^{R_{\rm max}} \frac{d^3\mathbf{r}'}{4\pi} \frac{\delta_{\rm g}(\mathbf{r}')(\mathbf{r}' - \mathbf{r})}{(\mathbf{r}' - \mathbf{r})^3} + \mathbf{V}_{\rm ext}, \tag{1.22}$$

where $R_{\rm max}$ corresponds to the survey depth, $\mathbf{V}_{\rm ext}$ encapsulates velocity contributions from structures beyond $R_{\rm max}$, and where we have defined $\beta \equiv f(\Omega_{\rm m})/b$. For a ΛCDM Universe, the growth rate of structure is given by $f = \Omega_{\rm m}^{0.55}$ (Wang & Steinhardt, 1998). Comparing measured PVs to predictions from a redshift survey thus in principle enables a measurement of $\beta = \Omega_{\rm m}^{0.55}/b$. Furthermore, one can obtain a measurement of the root-mean-square density of galaxies on an 8 h^{-1}Mpc scale directly from the redshift survey. By combining $\sigma_{8,\rm g}$ with the measured value of β, a constraint can be placed on the survey independent degenerate parameter combination $\sigma_8\Omega_{\rm m}^{0.55}$.

In addition to constraints placed on these parameters, when full sky surveys are used one can readily compute the velocity of the LG arising from the volume under consideration as predicted by linear theory. As the motion of the LG gives rise to the observed dipole in the CMB (Planck Collaboration et al., 2013c), a deviation from the predicted value with that inferred from the CMB dipole would presumably arise from sources beyond the survey and would thus have implications for large-scale structure. As the tidal field falls off as r^{-3}, to first order additional velocity contributions at the LG arising from sources outside the survey volume can be modelled as a dipole, with the magnitude of the dipole itself being a test for cosmological models. Furthermore, once the parameters of Equation (1.22) are determined, we obtain PV predictions for all the locations within the volume spanned by the survey. A volume weighted average of the velocity field then allows us to probe the underlying distribution of dark matter. Specifically, the mean square velocity of a volume of scale R probes the amplitude of the matter power spectrum (the Fourier transform of the two-point correlation function). This relation is commonly written

$$\langle v^2(R)\rangle = \frac{\Omega_{\rm m}^{1.1}}{2\pi^2}\int_0^\infty P(k)\tilde{W}^2(kR)dk, \tag{1.23}$$

where $P(k)$ is the power spectrum of mass fluctuations, and where $\tilde{W}(kR)$ is the Fourier transform of a window function of scale R (typically a sphere of radius R). As is apparent from Equation (1.23), bulk flow measurements are valuable tools which can be used to challenge cosmological models.

1.6.2 Foundational Work & Past Results

Early work using peculiar velocity measurements attempted to account for the observed CMB dipole by constraining the infall velocity of the Local Group (LG) towards the nearby Virgo Cluster ($\sim$15 h^{-1}Mpc away) (Yahil et al., 1980; Schechter, 1980; de Vaucouleurs & Peters, 1981; Aaronson et al., 1982). These measurements, however, found the infall of the LG to be $\sim$100-350 km s^{-1}, towards $l \simeq 270°$, $b \simeq 75°$, being of insufficient amplitude and direction to account for the motion as inferred from the CMB ($\sim$630 km s^{-1} towards $l \simeq 276°$, $b \simeq 29°$). The general consensus at the time was that the Hydra-Centaurus Supercluster ($\sim$40 h^{-1}Mpc away, in approximately the same direction as the CMB dipole) likely accounts for the majority of the residual motion (Lilje et al., 1986). This view changed dramatically in the late 1980s when the "7 Samurai" (7S) measured the mean motion of 400 bright elliptical galaxies ($\langle R\rangle \simeq 30\ h^{-1}$Mpc) to be 600 ± 100 km s^{-1} towards $l = 312° \pm 11°$, $b = 6° \pm 10°$ (Dressler et al., 1987). As Hydra-Centaurus was observed to participate in this motion, it suggested that the majority of the LG's motion must arise from massive structures beyond $\sim$50 h^{-1}Mpc, the very existence of which was in conflict with predictions from then popular models of large-scale structure formation (Vittorio et al., 1986). Although the amplitude of this measurement was later reduced by considering only objects at distances greater than $\sim$30 h^{-1}Mpc, Lynden-Bell et al. (1988) found that a significant amount of the LG's motion could be explained by the existence of a large structure at a distance of $\sim$45 h^{-1}Mpc they dubbed the "Great Attractor" (GA). Although upcoming redshift surveys would soon find excess galaxy number counts in that general vicinity (Dressler, 1988; Strauss & Davis, 1988), confirmation that this structure sourced the measured bulk flow of the 7S would require detection of a back-side infall using peculiar velocity measurements. The only tentative detection reported of such an infall (Dressler & Faber, 1990) was controversial (Burstein et al., 1990; Mathewson & Ford, 1994), with the work of Hudson (1994b) soon thereafter favouring a bulk flow encompassing this structure.

Velocity-Velocity Comparisons

With the acquisition of deep redshift surveys spanning a substantial portion of the sky, Equation (1.22) enabled a means of obtaining predictions for the underlying velocity field. The first reported constraint on β obtained in this manner was that of Strauss (1989). In

his analysis the all-sky Infrared Astronomical Satellite (IRAS) redshift survey composed of 2636 galaxies with a characteristic depth of 35 h^{-1}Mpc was used. Predicted velocities derived from this field were compared to the inhomogeneous Mark II catalogue composed of ∼430 velocity measurements, and a value of $\beta \sim 0.8$ was obtained. This methodology was refined in the early 1990s to include a procedural means of obtaining self-consistent true spatial positions and velocities of galaxies from measured redshifts (Yahil et al., 1991a). Noteworthy work at this time also included that of "Handsome Hudson" (Hudson, 1994a). Comparing the density field of 12,350 optically selected galaxies within 80 h^{-1}Mpc (see Hudson 1993) to velocities from Mark II, a value of $\beta = 0.50 \pm 0.06$ was obtained. Furthermore, by modelling the external velocity contribution as a dipole and fitting for its components, a residual bulk flow of 405 ± 25 km s^{-1} towards $l \simeq 292°$, $b \simeq 7°$ was found to arise from structures beyond 80 h^{-1}Mpc. We end this review on early work by mentioning the novel technique employed by Nusser & Davis (1995) in which they predict the radial peculiar velocity field expanded in spherical harmonic and Bessel functions from IRAS surveys. In combination with a spiral galaxy's measured flux, the β dependent predicted PVs are used to obtain a prediction for the spiral's luminosity. The scatter in the TF relation is then minimized for both the TF parameters and β, meaning *a priori* calibration of the TF relation is not required.

With a few notable exceptions (*e.g.* Lavaux et al. 2010), the methods developed and employed at this time for the purpose of velocity comparisons have remained largely unchanged. Analysis of this nature is data driven, and as such, publications in this field are generally aligned with the release of new redshift or peculiar velocity surveys. As Equation (1.22) is over all space, deep all-sky surveys are ideal for deriving velocity predictions. Two such surveys in the past 15 years have been used extensively for this purpose: the IRAS Point Source Catalogue Redshift Survey (PSCz, Saunders et al. 2000), and the Two-Micron All-Sky Survey (2MASS) Redshift Survey (2MRS, Huchra et al. 2012). PSCz is a 60 μm flux-limited, sparsely sampled redshift catalogue composed of 15,411 IRAS galaxies, and covering 84% of the sky. The most recent 2MRS is a densely sampled all-sky catalogue composed of ∼45,000 galaxies with $K_s \leq 11.75$, and covering 91% of the sky. Most recent studies involving PV predictions generally use 2MRS (Pike & Hudson, 2005; Erdoğdu et al., 2006; Lavaux et al., 2010; Davis et al., 2011; Branchini et al., 2012), with the tightest constraints to date (12%, Davis et al. 2011) arising from comparison of the 2MRS density field with SFI++, a homogeneously derived I-band Tully-Fisher catalog (Springob et al., 2007).

Motion of the Local Group

By analyzing the dipole anisotropy of an all-sky X-ray-selected cluster sample Kocevski & Ebeling (2006) claimed that only 44% of the LG's motion arises from the Great Attractor. The remaining 56% of the Local Group's motion was believed to result from structures between 130 and 180 h^{-1}Mpc, the most prominent of which is the Shapley Supercluster at a distance of ∼150 h^{-1}Mpc. Recent attempts to account for the motion of the Local Group

include that of Erdogdu et al. (2006) and Bilicki et al. (2012) in which they analyzed the growth of the flux-weighted dipoles from 2MRS ($K_s \leq 11.25$), and the 2MASS Extended Source Catalogue ($K_s \leq 13.5$), respectively. Although the value of β is obtained in these analyses by assuming convergence of the LG's amplitude, both groups found a large misalignment with the CMB dipole ($\sim$20°) at a distance of $\sim$130 h^{-1}Mpc. Erdogdu et al. (2006) accounted for this fact in part by suggesting that non-linear effects may play an important role in dipole determinations. Lavaux et al. (2010) have recently extended their analysis to the non-linear regime using a novel orbit-reconstruction algorithm to predict motions of nearby objects. Using the 2MRS density field, however, they similarly found a large misalignment angle ($\sim$45°) towards the edge of their data ($\sim$150 h^{-1}Mpc, see Figure 1.1), and suggested that better agreement may require greater survey depth in order to fully capture the prominent Shapley and Horologium-Reticulum Superclusters. To date, the the motion of the Local Group as inferred from the CMB has not been recovered.

Bulk Flows

As discussed above, the volume weighted mean of the velocity field probes the power spectrum of mass fluctuations. Bulk flow measurements can be obtained from PVs alone, and as mentioned, there is a rich history of developments in this field. Since the somewhat large value found by the 7S, results have remained somewhat mixed. While some recent measurements find consistency with ΛCDM (Dai et al., 2011; Nusser & Davis, 2011; Turnbull et al., 2012), others suggest existence of a large bulk flow in conflict with ΛCDM (Kashlinsky et al., 2008; Watkins et al., 2009; Colin et al., 2011). Although some of these measurements are potentially in conflict with ΛCDM, comparison of the measurements alone (with the exception of Kashlinsky et al. (2008)), show reasonable agreement in both direction and amplitude (see Table 1.1). Regarding the possibility of a conflict with ΛCDM, however, a consensus has yet to be reached.

Table 1.1: Qualitative comparison of recent bulk flow measurements on various scales using either spherical or Gaussian window functions. Aside from Kashlinsky et al. (2008), many of the datasets used in each study overlap.

	Scale (h^{-1}Mpc)	$\|\|\mathbf{v}\|\|$ (km/s)	l (°)	b (°)
Nusser & Davis (2011)	40	333 ± 38	276 ± 3	14 ± 3
Watkins et al. (2009)	50	407 ± 81	287 ± 9	8 ± 6
Turnbull et al. (2012)	40	249 ± 76	319 ± 18	7 ± 14
Colin et al. (2011)	160	260 ± 150	298^{+62}_{-48}	8^{+34}_{-52}
Dai et al. (2011)	150	188^{+199}_{-103}	290^{+39}_{-31}	20 ± 32
Kashlinsky et al. (2008)	300-800	600-1000	283 ± 18	12 ± 14

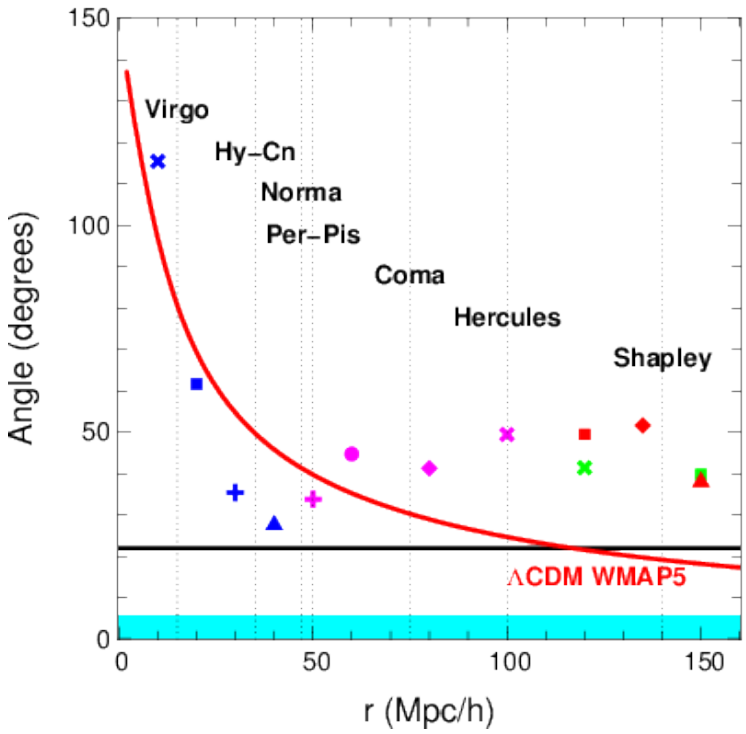

Figure 1.1: Reproduction of Figure 5 from Lavaux et al. (2010). Misalignment angle between the reconstructed Local Group velocity and CMB dipole is plotted. The velocity of the LG was obtained using a non-linear orbit reconstruction algorithm and 2MRS. The red curve represents a 95% probability limit of the misalignment angle for a ΛCDM Universe (assuming WMAP5 parameters). The cyan band gives the 1σ uncertainty on the measured direction of the CMB dipole, whereas the solid black line gives the 95% probability limit on the misalignment of the reconstructed velocity with the observed motion of the LG.

1.6.3 Thesis Overview & Outline

In this work we use the recently constructed all-sky 2M++ redshift catalogue composed of 69,160 galaxy redshifts, superior in both sky coverage and completeness to 2MRS. Following the work of Yahil et al. (1991a), we self-consistently reconstruct the local real-space density field from redshift space. We then compare predicted velocities from this field to measured velocities from the First Amendment SNe Ia dataset, as well as the current standard: SFI++, in order to constrain β, and in turn $\sigma_8\Omega_{\rm m}^{0.55} = \beta\sigma_{8,\rm g}$. As 2M++ contains supercluctures that have yet to be included in such an analyses (*e.g.* Shapley, Horologium) we check the growth of the LG's dipole arising from structures within 200 h^{-1}Mpc for convergence with the motion as inferred from the CMB dipole. To account for velocity contributions beyond 2M++ we follow Hudson (1994a) and simultaneously fit for an external dipole while measuring β. In an attempt to shed new light on the conflicting results of the past, we in turn measure the bulk flow on a range of scales and compare our findings to expectations of ΛCDM.

This work is organized as follows: in Chapter 2 we review construction of the 2M++ catalogue, outline methods used to account for incompleteness, account for functional dependence of bias on luminosity when computing the density field, and outline the reconstruction procedure. In Chapter 3 we discuss peculiar velocity datasets used, and outline methods for comparing predicted velocities to measured velocities. Key results are reported in Chapter 4, where we also discuss and compare results to those from recent literature. We conclude in Chapter 5 and discuss possible future extensions of this work. Appendix A reports results from an N-body simulation used to quantify any possible bias introduced as a result of smoothing kernel selection or density field reconstruction. In Appendix B we outline a more sophisticated biasing scheme and report preliminary results therefrom.

The bulk of this work (Chapters 2-5, Appendix A) is taken from the recently submitted J. Carrick *et al.* (2014). Appendix B is comprised of investigative work which may instigate a future publication. Unless otherwise stated, all text is the original work of this author.

Chapter 2

Density Field Reconstruction

Redshift surveys measure positions of objects in *redshift-space*. As Equation (1.22) requires *real-space* coordinates, we must first map observed redshifts to real-space positions. The observed redshift is related to cosmological redshift resulting from the expansion of the Universe and that resulting from peculiar velocities through Equation (1.15). The comoving distance in the low-redshift Universe can then be obtained from the cosmological redshift through Equation (1.18). As real-space positions are dependent on peculiar velocity predictions, which are themselves dependent on real-space positions, mapping redshifts to real-space must be done with care.

In this chapter we discuss the 2M++ redshift catalogue, and outline the procedure used in reconstructing comoving positions of the galaxies therein. We review construction of 2M++ in §2.1. In §2.2 we outline how galaxy weights were computed to account for the fact that 2M++ is magnitude limited. In §2.3 we briefly review choice of smoothing kernel. We discuss the procedure used to normalize the smoothed density field to the same effective bias in §2.4. In §2.5 we outline the iterative scheme used to recover real-space positions from redshift-space. Finally, in §2.6 we take a cosmographic tour through the recovered density field for the best value of β^*.

2.1 2M++ Redshift Compilation

The integral in Equation (1.8) is over all space. In reconstructing the velocity field of the local Universe, therefore, clearly one would like a redshift survey that is very deep and as close to full-sky as possible. Two such catalogues which have been used extensively in the past include the sparsely sampled IRAS Point Source Catalogue Redshift Survey (PSCz, Saunders et al. 2000), and more recently, the shallower but more densely sampled Two-Micron All-Sky Redshift Survey (2MRS, Huchra et al. 2012). In this work we use a superset of 2MRS constructed by Lavaux & Hudson (2011), which has greater depth than 2MRS, and superior sampling than PSCz. The photometry is based primarily from the

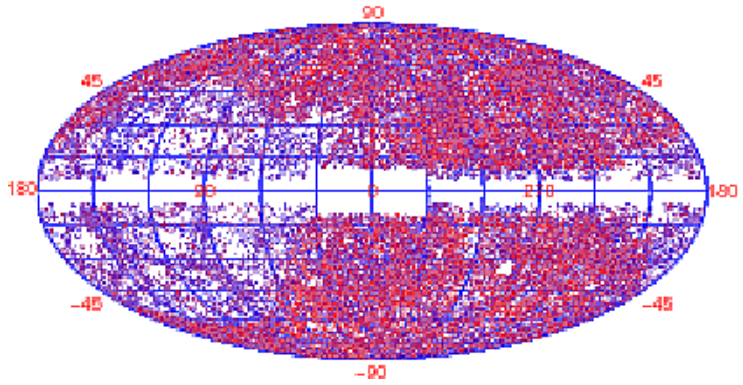

Figure 2.1: All galaxies in 2M++ with measured redshifts; blue galaxies are nearest, red are farthest.

Two-Micron-All-Sky-Survey (2MASS) Extended Source Catalogue, (2MASS-XSC, Skrutskie et al. 2006), an all-sky survey in the J, H and K_S bands. Redshifts in the K_S band of the 2MASS Redshift Survey (2MRS) are supplemented by those from the Sloan Digital Sky Survey Data Release Seven (SDSS-DR7, Abazajian et al. 2009), and the Six-Degree-Field Galaxy Redshift Survey Data Release Three (6dFGRS, Jones et al. 2009). Data from SDSS was matched to that of 2MASS-XSC using the NYU-VAGC catalogue (Blanton et al., 2005). As 2M++ draws from multiple surveys, galaxy magnitudes from all sources were first recomputed by measuring the apparent magnitude in the K_S band within a circular isophote at 20 mag arcsec^{-2}. Following a prescription described in Lavaux & Hudson (2011), magnitudes were then corrected for Galactic extinction, cosmological surface brightness dimming and stellar evolution. After corrections the sample was limited to $K_{2M++} \leq 11.5$ in regions not covered by 6dFGRS or SDSS, and limited to $K_{2M++} \leq 12.5$ elsewhere.

Other relevant corrections which were made to this catalogue include accounting for incompleteness due to fibre-collisions in 6dF and SDSS, as well as treatment of the *zone of avoidance* (ZoA). Incompleteness due to fibre-collisions was treated by cloning redshifts of nearby galaxies within each survey region as described in Lavaux & Hudson (2011).

In treating the ZoA, for Galactic longitudes in the range [30°, 330°], lower latitudes ($|b|$ <5°) were first masked and then filled with the redshifts from 2MRS lying exactly 5° above positive latitudes, and 5° below for negative latitudes. For longitudes in the range [-30°, 30°], latitudes $|b|$ <10° were filled with the redshifts from 6dFGRS lying 10° above positive latitudes, and 10° below for negative latitudes. Redshift distributions of the 2M++ catalogue is shown in Figure 2.1.

2.2 Luminosity Function & Galaxy Weights

Before using the catalogue to construct the density field, we must first account for survey incompleteness. In this section we provide a summary of the method used to obtain the luminosity function fit to the catalogue; this luminosity function is in turn used in the weighting scheme employed to account for incompleteness. For a complete description of these calculations as applied to this catalogue see Lavaux & Hudson (2011). The luminosity function used to characterize the dataset is the Schechter function (1976), which when written in terms of absolute magnitudes is given by:

$$\begin{aligned}\Phi(M) = \\ 0.4\log(10)n^*10^{0.4(1+\alpha)(M^*-M)}\exp\left(-10^{0.4(M^*-M)}\right),\end{aligned} \tag{2.1}$$

where n^* is the density normalization, M^* is the absolute magnitude break, and α is additional power-law parameter to be determined. Schechter function parameters are computed using likelihood formalism, where the product of all conditional probabilities of observing galaxies intrinsic magnitudes is maximized given their redshift, Schechter parameter values, and survey completeness at their specified angular positions and distances.

Before computing weights we must first discuss the different ways by which we can model the galaxy density contrast. As we cannot compute the mass density contrast of observed galaxies directly, we must use either the number-density of galaxies, or their luminosity-density in computing $\delta_{\rm g}$. Our goal is to create a galaxy density contrast field which most closely traces the underlying total mass density contrast in the context of linear biasing. Although luminosity-density may be a better proxy for stellar mass, and thus for the underlying distribution of dark matter, we will consider both schemes in this work.

To account for incompleteness, galaxies are weighted according to a common prescription similar to that of Davis & Huchra (1982). In the case of a number-density scheme, observed galaxies are weighted to account for the number of galaxies not observed at a given distance due to the magnitude limit of the survey. When using the galaxy number-density for a single homogeneous redshift survey, galaxies are weighted by

$$w^N(r) = \frac{N_{\rm average}}{N_{\rm observed}(r)} = \frac{\int_{L_{\rm min}}^{\infty}\Phi(L)\,dL}{\int_{4\pi r^2 f_{\rm min}}^{\infty}\Phi(L)\,dL}\,, \tag{2.2}$$

when $4\pi d_{\rm L}^2 f_{\rm min} > L_{\rm min}$, and unity otherwise.

In the event that the luminosity-density is used in computing the galaxy density contrast, the weight assigned to each galaxy's luminosity is again based on the fraction of the total luminosity expected given the magnitude limit of the survey, to the luminosity one expects to observe at a given distance. Thus, for a single homogeneous redshift survey, galaxy luminosities are weighted by

$$w^L(r) = \frac{L_{\rm average}}{L_{\rm observed}(r)} = \frac{\int_{L_{\rm min}}^{\infty}L\,\Phi(L)\,dL}{\int_{4\pi r^2 f_{\rm min}}^{\infty}L\,\Phi(L)\,dL}\,, \tag{2.3}$$

when $4\pi d_{\rm L}^2 f_{\rm min} > L_{\rm min}$, and unity otherwise. The actual weights used in this work must account for the inhomogeneous incompleteness of 2M++, and a full description of their determination can be found in Lavaux & Hudson (2011).

2.3 Smoothing

In order to make use of Equation (1.22), the density field must first be sufficiently smooth for linear theory to apply. The optimal scale on which to smooth the data was determined by comparing velocities from an N-body simulation to predictions obtained through linear theory using different smoothing lengths. Smoothing the density contrast with a 4 h^{-1}Mpc Gaussian was found to be the best compromise in minimizing the scatter in predicted velocities vs. simulation velocities, while simultaneously returning the slope expected in the relation. See Appendix A for further details.

2.4 Accounting for Magnitude Dependence of Galaxy-Matter Bias

For magnitude limited surveys such as 2M++, the mean luminosity of observed galaxies increases with depth. As galaxy-matter bias has been found to increase with luminosity, this means that objects observed at higher redshift are on average more biased than those observed nearby. In this section we account for this effect by scaling the density field to the same effective bias. We do so using the scaling relation model in Westover (2007). By comparing the correlation function of 2MASS volume-limited subsamples, converting the mean absolute magnitude of the bin to a luminosity and defining $b/b^* = (\xi(z)/\xi_{\rm fid}(z))^{1/2}$, Westover (2007) found $b/b^* = (0.73 \pm 0.07) + (0.24 \pm 0.04) L/L^*$, where b^* is the bias of an L^* galaxy. This result is consistent with that of Norberg et al. (2001) and Tegmark et al. (2002), who did similar analyses using projected correlation functions of 2dFGRS and the SDSS power spectrum, respectively.

As our end goal is to compare predicted velocities with measured velocities and determine f/b, we must first correct the density contrast field by normalizing the field to the same effective bias. The effective number-weighted bias is computed as follows:

$$b_{\rm eff}^N(r) = \frac{\int_{4\pi r^2 f_{\rm min}}^{\infty} b(L)\, \Phi(L)\, dL}{\int_{4\pi r^2 f_{\rm min}}^{\infty} \Phi(L)\, dL} = \psi^N(r) b^*. \tag{2.4}$$

Using a luminosity-weighting scheme in computing the density contrast, the effective luminosity-weighted bias is given by:

$$b_{\rm eff}^L(r) = \frac{\int_{4\pi r^2 f_{\rm min}}^{\infty} b(L)\, L\, \Phi(L)\, dL}{\int_{4\pi r^2 f_{\rm min}}^{\infty} L\, \Phi(L)\, dL} = \psi^L(r) b^*. \tag{2.5}$$

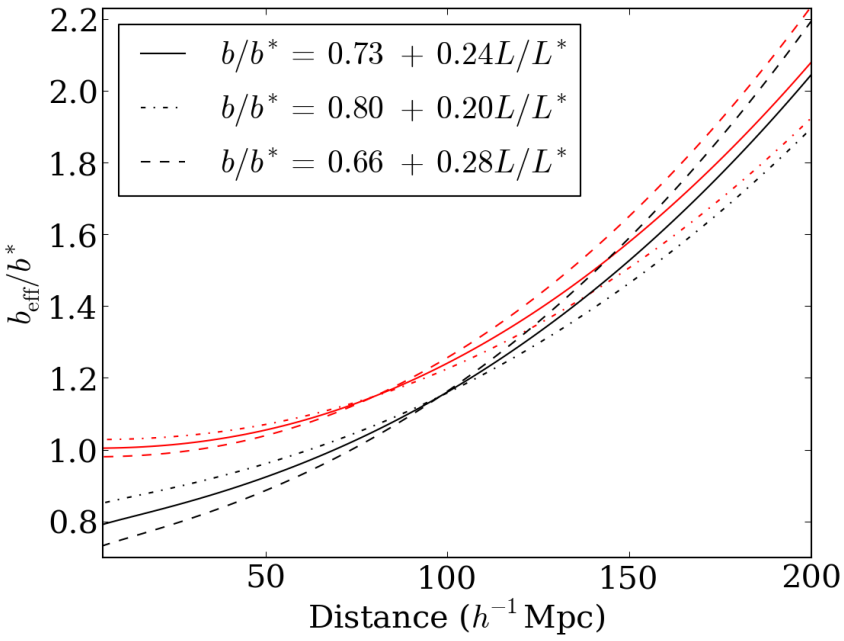

Figure 2.2: Number-weighted (lower) and luminosity-weighted (upper) effective bias as a function of distance for the most significant 1σ deviation of parameters from the scaling relation $b/b^* = (0.73 \pm 0.07) + (0.24 \pm 0.04)L/L^*$. Plots are obtained using the parameter values $\alpha = -0.85$ and $M^* = -23.25$ for the Schechter luminosity function.

Using the functional form of $b(L)$ quoted above from Westover (2007), this normalization procedure was applied to the 2M++ density contrast fields. Both the number-weighted and luminosity-weighted effective bias for $\alpha = -0.85$, $M^* = -23.25$, and a magnitude limit of 12.5 are shown in Figure 2.2. We can then rewrite Equation (1.22) as

$$\mathbf{v}(\mathbf{r}) = \frac{\beta^*}{4\pi} \int d^3\mathbf{r}' \delta_{\rm g}^*(\mathbf{r}') \frac{(\mathbf{r}' - \mathbf{r})}{|\mathbf{r}' - \mathbf{r}|^3} \,, \tag{2.6}$$

where we have defined $\beta^* \equiv f(\Omega)/b^*$, and $\delta_{\rm g}^*(r) \equiv b^*\delta(r) = \delta_{\rm g}(r)/\psi(r)$.

2.5 Reconstruction Procedure

Reconstructing real space distances to catalogue objects was accomplished via an iterative procedure modeled on that of Yahil et al. (1991b). Objects were first grouped using the "Friends-of-friends" algorithm (Huchra & Geller, 1982), and then placed at the mean of their group redshift distance to stifle the "Fingers-of-God" effect. Gravity was then adiabatically turned on by increasing $\beta^* \equiv f(\Omega_{\rm m})/b^*$ from 0 to 1.00 in steps of 0.01. The

reconstruction took place in the LG frame, and on each iteration the following steps were taken:

1. Schechter luminosity function is fitted to the data using the likelihood formalism discussed in §2.2. The LF is in turn used to compute either the luminosity or number weights following the procedure mentioned in §2.2.

2. Galaxies from 2MRS with distances greater than 12,500 km s^{-1} are assigned a weight of zero. Galaxy properties, including newly computed weights are then cloned to account for incompleteness and fill the ZoA as described in §2.1.

3. Number weighted galaxies or their weighted luminosities within 20,000 km s^{-1} are then placed on a grid of 257^3.

4. The density contrast field is then normalized to the same bias, b^*, as described in §2.4. The field is in turn smoothed with a Gaussian kernel of width 4 h^{-1}Mpc.

5. The velocity field is then computed from which the peculiar velocity of all objects in the catalogue are obtained.

6. Predicted peculiar velocities projected on to the line-of-sight are then weighted by the value of β^* at that step in the iteration and used in conjunction with LG frame redshifts to obtain a new prediction for their comoving distance using Equations (1.15) and (1.18).

7. The previous five predictions for a galaxy's distance are then averaged to stifle the impact of triple-valued regions. The averaged distance is in turn assigned to the galaxy and used to recompute the galaxy's absolute magnitude. Computed distances and magnitudes are then used in the subsequent iteration.

Catalogues containing updated distances and magnitudes were saved at each iteration in addition to the computed density and velocity fields.

It should be noted that this iterative reconstruction procedure was found to be unbiased in determining the best fit value of β when the full analysis was run on an N-body simulation using a ΛCDM cosmology (see Appendix A for more details).

2.6 Cosmography

Figure 2.3 shows the luminosity-weighted density field of the Supergalactic Plane for $\beta^* = 0.43$, smoothed with a 4 h^{-1}Mpc Gaussian kernel. The incomplete coverage due to the lower magnitude limit of 2MRS is clearly visible in this figure beyond SGX $\simeq$ 75 h^{-1}Mpc. The most prominent overdensity in this plane is the Shapley concentration located at (SGX, SGY) $\simeq$ (-125, 75) h^{-1}Mpc. Other notable structures in Figure 2.3 include the Virgo

Supercluster directly above the LG, the Hydra-Centaurus Supercluster (-40, 12.5) h^{-1}Mpc and the Perseus-Pisces Suplercluster (40, -30) h^{-1}Mpc. Additional slices through SGZ are shown in Figure 2.4, though smoothed on a 7 h^{-1}Mpc scale to enhance the contrast of large overdensities. For instance, Horologium-Reticulum Supercluster can be readily observed at SGZ $\simeq$ -112 h^{-1}Mpc, SGX $\simeq$ -70 h^{-1}Mpc, SGY $\simeq$ -140 h^{-1}Mpc. The supergalactic plane is also shown with this smoothing for comparison.

2.7 2M++ Acceleration on the Local Group

The acceleration of the LG as predicted by linear theory for an ideal volume-limited catalogue is given by:

$$\mathbf{v}_{\rm LG} = \frac{\beta^*}{4\pi} \int_0^{R_{\rm max}} d^3\mathbf{r}' \delta_{\rm g}^*(\mathbf{r}') \frac{\mathbf{r}'}{r'^3} + \mathbf{V}_{\rm ext} \ , \tag{2.7}$$

where $\mathbf{V}_{\rm ext}$ encapsulates contributions from beyond $R_{\rm max}$, and to first order, can be approximated as a dipole. For a realistic flux-limited catalogue, we do not detect a continuous distribution of matter but a finite number of galaxies. As a result, our estimate of the acceleration of the LG using 2M++ is subject to sample variance. To estimate the effect of sample variance on our predicted motion of the LG, we computed the standard deviation in each of the components of 500 bootstrap samples. The sample variance in the amplitude of the LG's motion from this analysis was found to be 56 km s^{-1}.

Under the assumption that the observed CMB dipole arises from the motion of the LG, there has been much debate as to the structures sourcing this motion. Most recent work has made use of 2MASS-XSC or 2MRS in reconstructing the motion of the LG, and there has yet to be consensus on the distance at which the LG's motion coincides with that derived from the CMB. Erdoğdu et al. (2006) argue that more than 70% of the LG's motion results from structures within 500 h^{-1}Mpc, such as Hydra-Centaurus Supercluster. While others argue for convergence at distances greater than ∼150 h^{-1}Mpc such as Lavaux et al. (2010) using Monge-Ampère-Kantorovich orbit-reconstruction method, or Bilicki et al. (2011), who explored the convergence of the 2MASS dipole moment of the angular distribution of galaxies as a function of the limiting flux of the sample. As 2M++ is a superset of 2MRS and contains redshift measurements up to a magnitude limit of $K_{\rm s} = 12.5$, this data is well suited to examine the influence of structures beyond 150 h^{-1}Mpc on the acceleration of the Local Group.

Using density fields for different values of β^* that were obtained throughout the iteration procedure discussed in §2.5, the velocity field of increasingly larger concentric spheres centered on the LG was computed. The direction and amplitude of the LG's velocity as a function of distance for different values of β^* was then obtained. The amplitude of the LG acceleration as predicted by 2M++ for different values of β^* is shown in Figure 2.5. The expected agreement between predictions using linear theory for a survey of a certain depth with values derived from the CMB were computed for comparison. This conditional

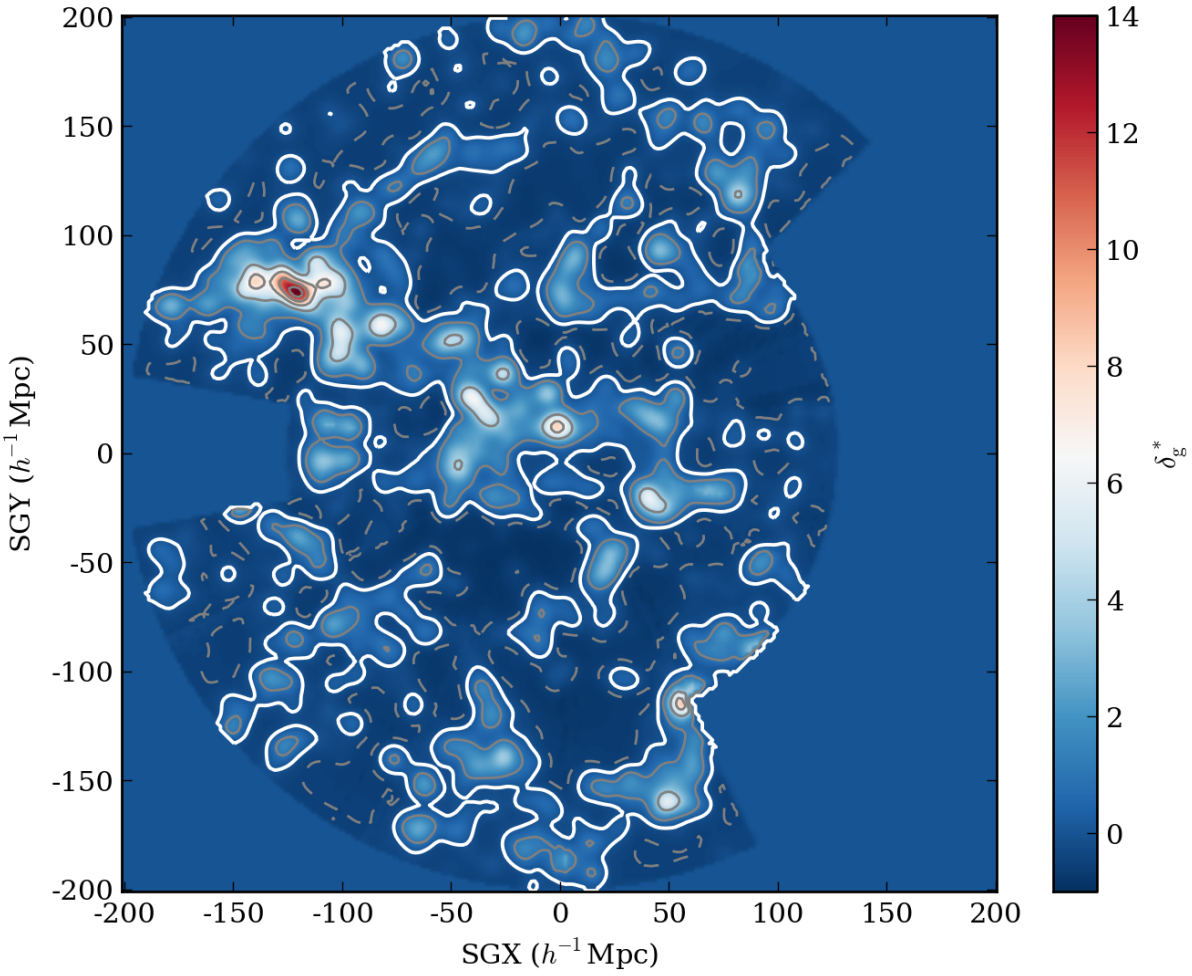

Figure 2.3: Density contrast of the supergalactic plane for $\beta^* = 0.43$ smoothed with a Gaussian kernel of radius 4 h^{-1}Mpc. The dashed contour is $\delta_g^* = -0.5$, the bold white contour is $\delta_g^* = 0$, and successive contours thereafter increase from 1 upwards in steps of 3.

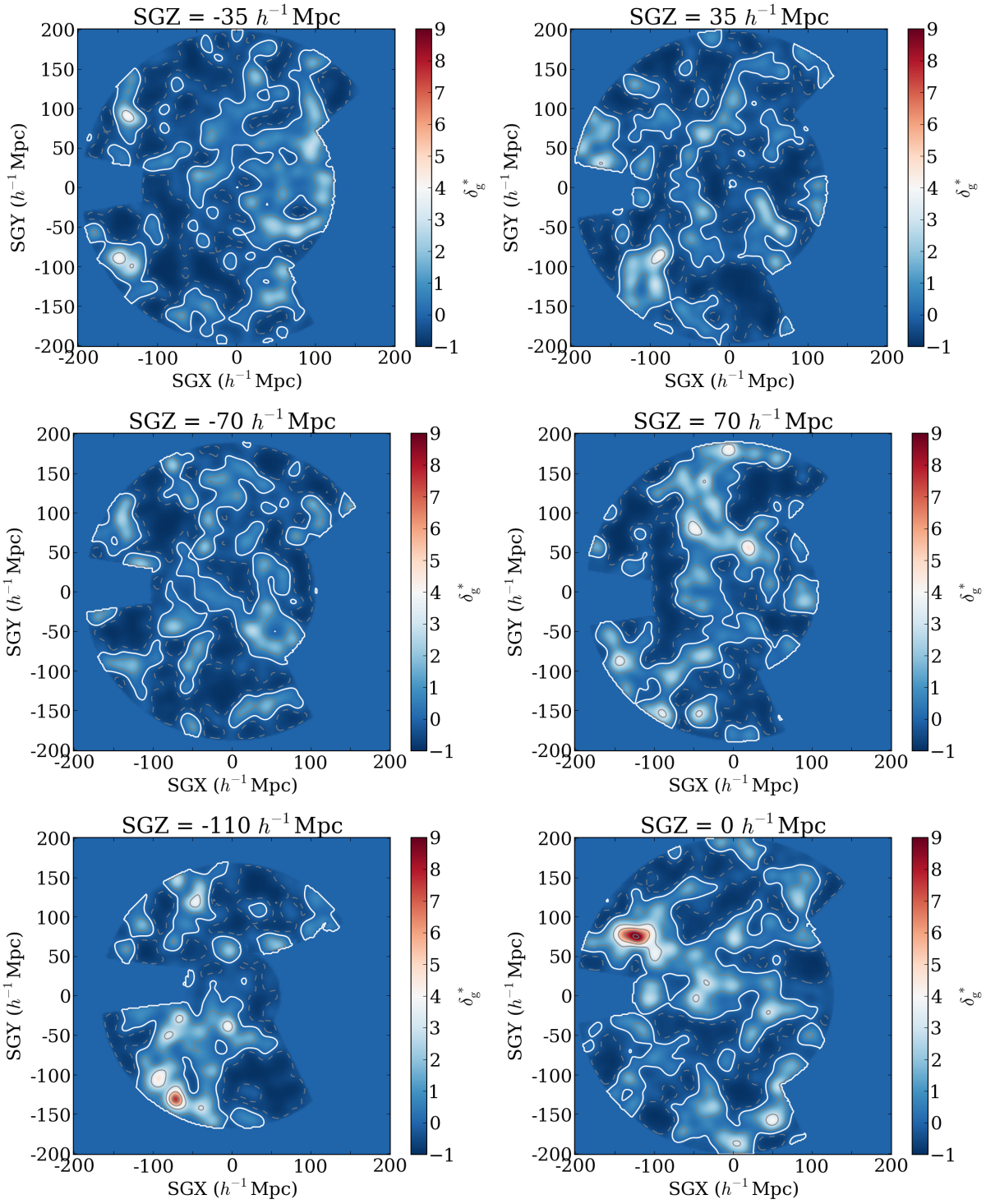

Figure 2.4: The 2M++ density field at various slices of SGZ. The density field was smoothed with a 7 h^{-1}Mpc Gaussian kernel. The dashed contour is $\delta_g^* = -0.5$, the bold white contour is $\delta_g^* = 0$, and successive contours thereafter increase from 1 upwards in steps of 2.

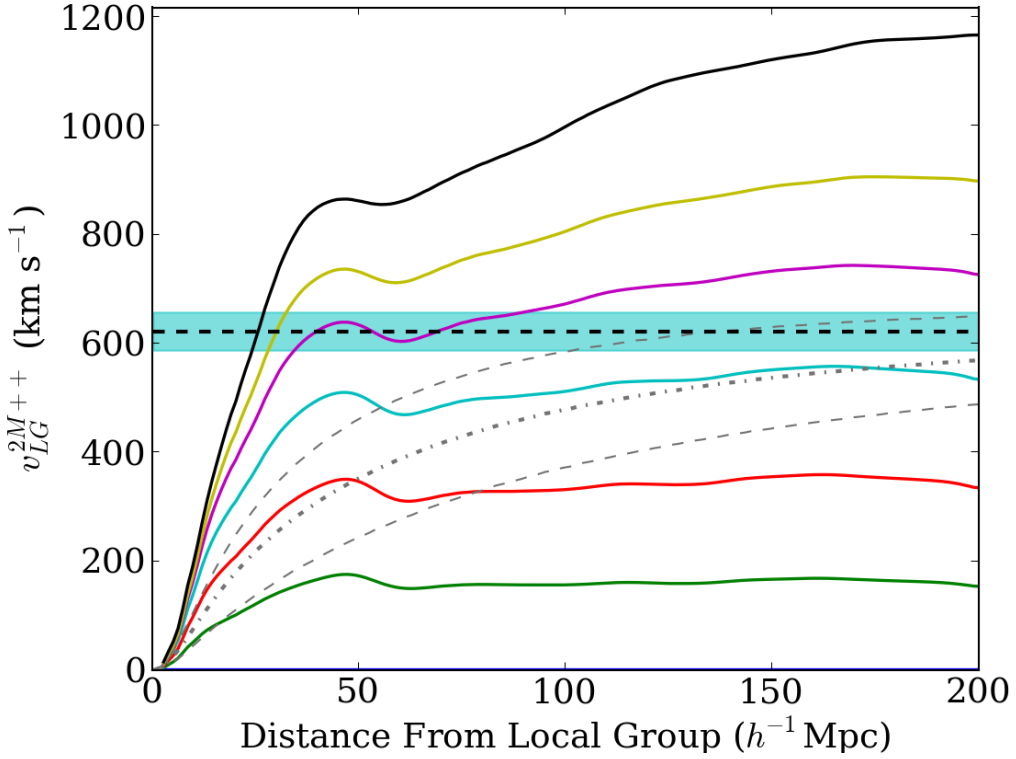

Figure 2.5: Growth of LG velocity amplitude as predicted by linear theory for successively larger concentric spheres as a function of radius for various steps in the iterative reconstruction. The solid lines correspond to predictions from linear theory, the dash-dot lines correspond to the expected velocity amplitude and angular agreement that would be measured for a survey of a depth indicated by the x-axis for a ΛCDM WMAP5 cosmology. The shaded cyan band corresponds to the velocity of the Local Group as inferred from the CMB dipole. Uncertainties plotted are 68% confidence intervals.

probability assumes a ΛCDM WMAP5 cosmology. A derivation of this conditional velocity can be found in Appendix A of Lavaux et al. (2010), and is based on Lahav et al. (1990). The convergence of the direction of LG velocity with that derived from the CMB ($l = 273° \pm 3°$, $b = 29° \pm 3°$) is plotted in Figure 2.6. For our best fit value of $\beta^*= 0.43$, the misalignment is 10°. This agreement is significantly better than those found by past studies using the shallower 2MRS, such as the 21° agreement found by Erdogdu et al. (2006), 19° found by Bilicki et al. (2011), or the $\sim 45°$ agreement found by Lavaux et al. (2010).

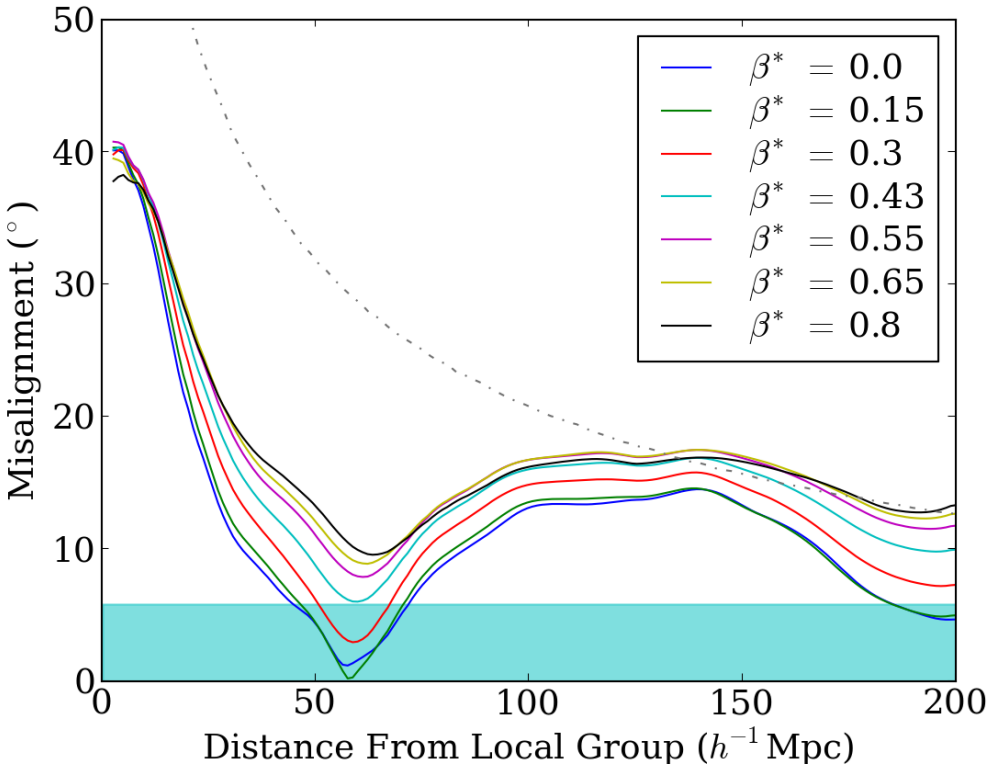

Figure 2.6: Misalignment of the LG predicted direction of the acceleration arising from 2M++ with that derived from the CMB ($l = 273°$, $b = 29°$), for different values of β^* as a function of radius. The solid lines correspond to predictions from linear theory, the dash-dot lines correspond to the expected velocity amplitude and angular agreement that would be measured for a survey of a depth indicated by the x-axis for a ΛCDM WMAP5 cosmology. The shaded cyan band corresponds to the velocity of the Local Group as inferred from the CMB dipole. Uncertainties plotted are 68% confidence intervals.

Chapter 3

Peculiar Velocity Comparisons

3.1 Peculiar Velocity Surveys

3.1.1 SFI++

SFI++ (Springob et al. 2007) builds primarily on Spiral Cluster I-band (SCI) and Spiral Field I-band (SFI) samples and uses a mixture of 21-cm line profile widths and optical rotation curves in determining the I-band Tully-Fisher (TF) relation from a subset of 807 galaxies in the fields of 31 clusters and groups Masters et al. (2006). From the derived TF relation they in turn determine the peculiar velocities of 5780 galaxies. Upon removing galaxies without high-quality width measurements and those that are located beyond the volume covered by 2M++, SFI++ can be divided in to two subsets of 2583 field galaxies and 735 galaxy groups.

As noted by Davis et al. (2011), the SFI++ TF relation has a kink in the faint end ($M > -20$), and an asymmetric distribution of outliers about the expected velocity width parameter $\eta \equiv \log(W) - 2.5$ (Springob et al. 2007), where W is two times the maximum rotation velocity (in km s^{-1}) corrected to edge-on inclination. As we will be fitting for the inverse TF relation, we will account for the outliers and deviation from linearity of the relation by excluding galaxies with redshift-distance magnitudes fainter than -20. We then iteratively compute the TF relation parameters and remove those with a velocity width that deviates by more than 0.2 (3.8σ) from the relation, until derived parameter values converge. Selection on both magnitude and velocity width resulted in the rejection of 503 field galaxies and 137 galaxy groups. Furthermore, when comparing predicted velocities from 2M++ with those from SFI++, the remaining objects which were found to differ by more than 3.5σ with all velocity fields obtained through the reconstruction procedure were rejected (0.6%). The final sample was composed of 2067 field galaxies and 595 galaxy groups and had uncertainty-weighted depths of 42 h^{-1}Mpc and 25 h^{-1}Mpc, respectively.

Before predictions are compared with velocities from SFI++ we first correct for the fact that the velocities were obtained under the assumption that $cz_{\rm obs} = H_0 R + v_{\rm pec}$. We

use instead the analytic relation from Equation (1.15) to obtain velocities from measured positions.

3.1.2 First Amendment

The First Amendment (A1) catalogue of Type Ia Supernovae (SNe) datasets compiled by Turnbull et al. (2012). A1 is composed of SNe within 200 h^{-1}Mpc and draws 34 SNe from Jha et al. (2007), 185 from Hicken et al. (2009) and 26 from Folatelli et al. (2010). Of these 245 SNe, 237 are within the volume spanned by 2M++, and have an uncertainty-weighted depth of 31 h^{-1}Mpc.

3.2 Velocity-Velocity Comparisons

For the SFI++ subsets we use the distances as determined in Springob et al. (2007) which have not been corrected for Malmquist bias. We similarly do not use Malmquist bias corrected A1 distances. Of the comparison methods discussed below, VELMOD is unaffected by inhomogeneous Malmquist bias, and accounts for homogeneous Malmquist bias in the likelihoods. The Forward Likelihood method discussed accounts for both homogeneous and inhomogeneous Malmquist bias in the likelihoods. The simple χ^2 comparison, however, neither accounts for homogeneous nor inhomogeneous Malmquist bias, and as such, the results yielded from this analysis are taken to be biased.

3.2.1 VELMOD

VELMOD is a rigorous maximum likelihood method first proposed and implemented by Willick et al. (1997) and described further in Willick & Strauss (1998). It is a velocity-velocity comparison method used to fit for the TF relation parameters (zero-point, slope and scatter) while simultaneously fitting for β^*. VELMOD takes as inputs TF parameters, an object's redshift and one of the observables (velocity-width or apparent magnitude), and maximizes the probability of observing one given the other. The strength of VELMOD analysis is that it neither assumes a one to one mapping from redshift space to real space (accounting for errors due to triple-valued regions), nor does it require calibration of the TF relation prior to its implementation.

Forward VELMOD uses the velocity-width to predict a galaxy's apparent magnitude, whereas the inverse method uses the apparent magnitude to predict the velocity-width parameter. The forward method is strongly dependent on selection effects, and thus requires a well-modeled selection function. The inverse method, however, is marginally dependent on selection effects due to sample selection's possible weak dependence on velocity-width. As the selection function of SFI++ is rather difficult to model accurately due to its being a compilation of various surveys with a range of selection criteria, we will make use

of the inverse method in our analysis. This analysis assumes a TF relation of the form $\eta^0(M) = -b_{\rm inv}^{-1}(M - a_{\rm inv})$, where $\eta = \log_{10}(W) - 2.5$, $M = m - 5\log(d_{\rm L}(r))$ is the absolute magnitude, $d_{\rm L} = (1 + z_{\rm cos})R$ is the luminosity distance, and where $b_{\rm inv}$, $a_{\rm inv}$ and σ_η are the slope, intercept and rms scatter of the inverse relation, respectively.

The conditional probability of observing a measured velocity-width of a galaxy with an apparent magnitude, m, and an observed redshift, z, is given by:

$$P(\eta|m, cz) = \frac{P(\eta, m, cz)}{\int_{-\infty}^{\infty} d\eta\, P(\eta, m, cz)}, \tag{3.1}$$

where

$$P(\eta, m, cz) = \int_0^\infty dr\, P(\eta, m|r)\, P(cz|r)\, r^2\,, \tag{3.2}$$

$$\begin{aligned} P(\eta, m|r) \propto\, & \Phi(m - \mu(r)) \times \\ & S(m, \eta, r) \exp\left(-\frac{[\eta - \eta^0(m - \mu(r))]^2}{2\sigma_\eta^2}\right), \end{aligned} \tag{3.3}$$

$$P(cz|r) = \frac{1}{\sqrt{2\pi\sigma_v^2}} \exp\left(\frac{-[cz - cz_{\rm pred}]^2}{2\sigma_v^2}\right), \tag{3.4}$$

$$(1 + z_{\rm pred}) = (1 + z_{\rm cos}(r))(1 + \beta^* u(r)/c), \tag{3.5}$$

where $z_{\rm cos}(r)$ is related to the comoving distance $r \equiv H_0 R$ through Equation (1.18), $S(m, \eta, r)$ is the selection function, u is the radial predicted velocity, σ_v is the scatter in the predicted velocity about linear theory, and where $\mu(r) \equiv 5\log r$ is the distance modulus. We can then compute the product of the conditional probability $P(\eta|m, cz)$ over all galaxies and minimize the quantity

$$\mathcal{L}_{\rm IV} = -2\sum_i \ln P(\eta_i|m_i, cz_i). \tag{3.6}$$

Before implementation of VELMOD we follow the magnitude correction discussed in Masters et al. (2006) to account for morphological dependence of the TF Relation.

3.2.2 Forward Likelihood

We use a maximum likelihood method first described in Pike & Hudson (2005) which was developed to compare peculiar velocities obtained through SNe surveys while accounting for triple valued regions. This method maximizes the probability of a galaxy having its observed redshift

$$P(cz) = \int_0^\infty dr P(cz|r)P(r)\,, \tag{3.7}$$

where

$$P(cz|r) = \frac{1}{\sqrt{2\pi\sigma_v^2}} \exp\left(\frac{-[cz - cz_{\rm pred}]^2}{2\sigma_v^2}\right), \tag{3.8}$$

$$(1 + z_{\rm pred}) = (1 + z_{\cos}(r, \widetilde{h}))(1 + \beta^* u(r)/c), \tag{3.9}$$

where $z_{\cos}$ is given through the relation

$$\widetilde{h}r = cz_{\cos}\left(1 - \frac{1+q_0}{2} z_{\cos}\right), \tag{3.10}$$

and where

$$P(r) \propto \exp\left(-\frac{[r-d]^2}{2\sigma_d^2}\right)[1 + \delta_{\rm g}^*(r)], \tag{3.11}$$

d is the distance as determined by the peculiar velocity survey, σ_d is the uncertainty is the measured distance, and $\widetilde{h}$ allows for a rescaling of the distance as published. The product of $P(cz)$ for all objects is then computed, from which the quantity $\mathcal{L}_{\rm FL} = -2\sum_i \ln P(cz_i)$ is minimized.

3.2.3 χ^2 Minimization

In addition to the comparison method discussed above we also perform a simple χ^2 minimization procedure to determine the best value of β^*. For this minimization procedure we compare the observed redshift of the object with the sum of its measured distance and predicted peculiar velocity at that distance, *i.e.*

$$\chi^2(\beta^*) = \sum_i \frac{(cz_i - cz_{\rm pred})^2}{\sigma_{d_i}^2 + \sigma_v^2}\,, \tag{3.12}$$

where $z_{\rm pred}$ is given by Equation (3.9). Note that this expression does not account for the effects of density inhomogeneities along the line of sight. The recovered value of β^* is affected by inhomogeneous Malmquist bias and results from this method are thus expected to be biased high as a result. Nevertheless, the χ^2 statistic is useful to assess goodness-of-fit and so is included here.

Chapter 4

Results & Discussion

4.1 Summary of Results

Key results obtained through velocity-velocity comparison methods discussed in §3.2 are summarized in Table 4.1. To determine the value of β^* at which $\mathcal{L}_{\rm FL}$ and χ^2 are minimized, a cubic function was fit to resultant data. Comparison of the TF relation constants ($a_{\rm inv}$, $b_{\rm inv}$) obtained to those found by Masters et al. (2006) are shown in Table 4.1. The best fit value for all parameters, including β^* and its errors were obtained from 500 bootstrap samples of both 2M++ and the peculiar velocity datasets. Through bootstrap analysis it was found that peculiar velocity datasets and 2M++ contributed essentially equal amounts to overall parameter errors. The value obtained for the best fit external dipole, $V_{\rm ext}$, is given in Table 4.1 along with the bulk flow (50 h^{-1}Mpc Gaussian weighted mean of the velocity field) and the predicted velocity of the LG arising from 2M++. A comparison of χ^2 with and without the fitted dipole results in a difference of 34 for the 3 degrees of freedom, the dipole model is thus preferred at the 5.1σ level.

For a qualitative illustration of the agreement of our velocity predictions with the measured values from SFI++ and A1 we have plotted the projected line-of-sight (LOS) velocity within a 30° cone centered on major superclusters in Figure 4.2, several of which lie near the direction of $\mathbf{V}_{\rm ext}$. From this figure it is apparent that predictions do in fact follow the trends observed in measured velocities. Furthermore, it is apparent that addition of $\mathbf{V}_{\rm ext}$ to predicted velocities seems to provide better agreement than predictions alone, suggesting that such a dipole is in fact warranted.

In combination with a measurement of $\sigma^*_{8,\rm g}$, β^* can be used to constrain the cosmology dependent (and survey independent) degenerate parameter combination $f\sigma_8 = \beta^*\sigma^*_{8,\rm g}$. To measure $\sigma^*_{8,\rm g}$ from 2M++ we follow a similar prescription to that of Efstathiou et al. (1990a), we compute $\sigma^*_{8,\rm g} = \langle\sigma_{8,\rm g}(r)/\psi(r)\rangle$ using counts in cells within radial shells. Using this maximum likelihood scheme we obtain the value $\sigma^*_{8,\rm g} = 0.99 \pm 0.04$, where the errors quoted are derived from the scatter among different shells (see Figure 4.1), as this value

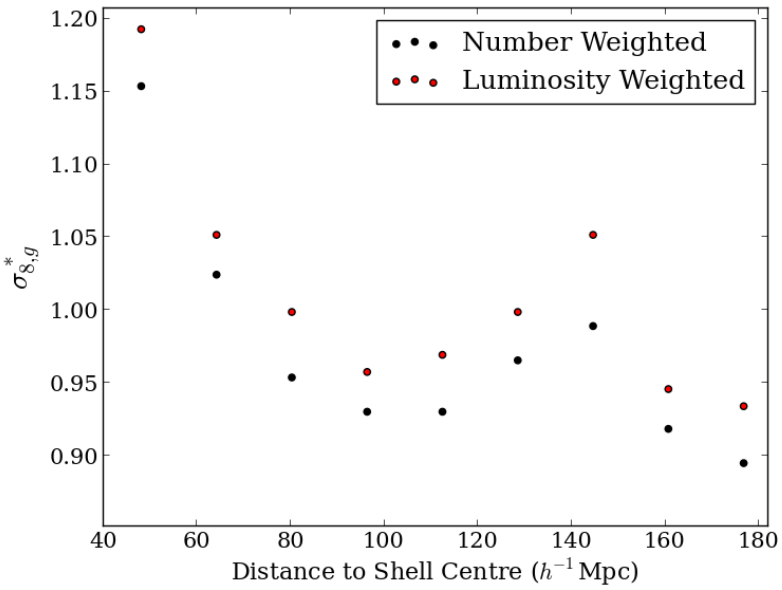

Figure 4.1: Bias corrected root-mean-square density fluctuations of galaxies on an 8 h^{-1}Mpc scale within radial shells of width 16 h^{-1}Mpc. Galaxy positions used are those which correspond to $\beta^* = 0.43$. Red points are luminosity density fluctuations (upper), whereas number density fluctuations are shown in black (lower).

Table 4.1: TF relation constants obtained through Inverse VELMOD analysis of SFI++ galaxies. Results listed are those obtained using a luminosity-weighting (LW) reconstruction scheme.

	$a_{\rm inv}$	$b_{\rm inv}$
Masters et al. (2006)	-20.881	-8.435
This Study	-20.918 ± 0.012	-8.19 ± 0.06

was found to be more conservative then the formal errors from the likelihood analysis. This value is in good agreement with that found by Westover (2007) of $\sigma^*_{8,\rm g} = 0.98 \pm 0.07$ obtained by fitting projected correlation functions to 2MRS galaxies within the magnitude range containing L^* galaxies, *i.e.* $-23.5 < K_s < -23.0$. The product of the growth factor and non-linear σ_8 is thus $f\sigma_8 = 0.427 \pm 0.026$. By adopting the value of $\Omega_{\rm m} = 0.3$, we can transform our non-linear value of σ_8 to a linearized value following the prescription of Juszkiewicz et al. (2010). We in turn obtain the constraint $f\sigma_{8,\rm lin} = 0.401 \pm 0.024$. It is important to note that linearization is only weakly dependent on the adopted value of $\Omega_{\rm m}$ ($\Omega_{\rm m} = 0.266$ results in $f\sigma_{8,\rm lin} = 0.398 \pm 0.024$). We compare these results with those obtained using independent methods in the following section.

Table 4.2: Summary of best fit values of β^* using different weighting schemes, methods of analysis and peculiar velocity datasets. Results obtained using luminosity weighting are indicated by (LW), whereas those obtained using number weighting are indicated by (NW). Unless explicitly indicated, all datasets were used for the method mentioned with the exception of Inverse VELMOD which used all individual galaxies from SFI++.

	β^*	χ^2/(D.O.F.)	$\hat{\mathbf{x}}\cdot\mathbf{V}_{\rm ext}$	$\hat{\mathbf{y}}\cdot\mathbf{V}_{\rm ext}$	$\hat{\mathbf{z}}\cdot\mathbf{V}_{\rm ext}$
Forward Likelihood (LW)					
A1	0.440 ± 0.023	-	94 ± 30	-128 ± 40	1 ± 29
SFI++ Galaxy Groups	0.429 ± 0.022	-	68 ± 35	-159 ± 35	19 ± 24
SFI++ Field Galaxies	0.423 ± 0.045	-	74 ± 37	-116 ± 40	30 ± 61
All	**0.431 ± 0.021**	-	**89 ± 21**	**-131 ± 23**	**17 ± 26**
Forward Likelihood (NW)	0.439 ± 0.020	-	131 ± 21	-90 ± 20	-51 ± 22
Inverse VELMOD (LW)	0.387 ± 0.048	-	42 ± 33	-232 ± 40	62 ± 28
χ^2 (LW)	0.444 ± 0.026	2194/2899	81 ± 27	-155 ± 30	-4 ± 24
χ^2 (NW)	0.442 ± 0.028	2200/2899	114 ± 29	-150 ± 30	-26 ± 28

Table 4.3: The bulk flow and motion of the LG arising from 2M++ for our best value of $\beta^* = 0.43$. The best dipole, $\mathbf{V}_{\rm ext}$, that was fitted simultaneously with β^* using the Forward Likelihood is also shown below. The bulk flow was computed by taking a 50 h^{-1}Mpc Gaussian weighted mean of the velocity field corresponding to $\beta^* = 0.43$.

	$v_{\rm x}$ (km s^{-1})	$v_{\rm y}$ (km s^{-1})	$v_{\rm z}$ (km s^{-1})	$\|\vec{v}\|$ (km s^{-1})	longitude (°)	latitude (°)
$\rm BF_{2M++}$	-3 ± 8	-72 ± 11	38 ± 11	81 ± 11	268 ± 6	28 ± 10
$\rm LG_{2M++}$	-18 ± 27	-422 ± 41	328 ± 37	535 ± 40	268 ± 4	38 ± 6
$\mathbf{V}_{\rm ext}$	89 ± 21	-131 ± 23	17 ± 26	159 ± 23	304 ± 11	6 ± 13
$\rm BF_{2M++} + \mathbf{V}_{ext}$	86 ± 22	-203 ± 26	55 ± 28	227 ± 25	293 ± 8	14 ± 10
$\rm LG_{2M++} + \mathbf{V}_{ext}$	71 ± 34	-553 ± 47	345 ± 46	656 ± 47	277 ± 4	32 ± 6

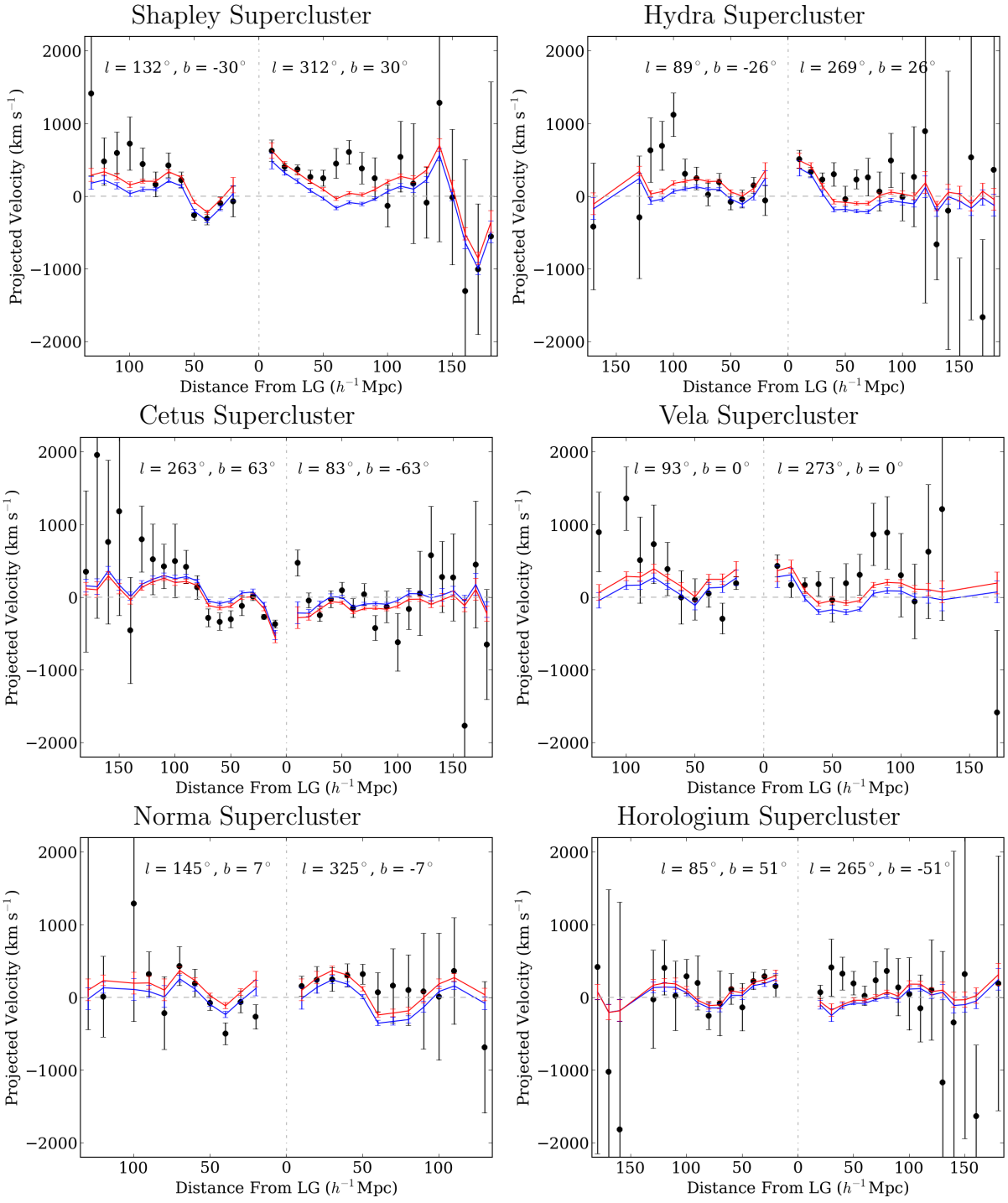

Figure 4.2: The velocity of all objects from A1 and SFI++ within a 30° cone of indicated direction. Velocities are projected on to the line-of-sight. Predictions used are those from 2M++ for our best value of $\beta^* = 0.43$, and are shown with (red) and without (blue) the preferred dipole. Points plotted are the error weighted mean of velocities within bins of 10 h^{-1}Mpc. To the left of the origin the negative value of the peculiar velocity is plotted.

4.2 Potential Systematic Effects

In this section we discuss the various effects which could bias our measurement of β^* and our prediction of the motion of the LG. Possible contributing factors include:

1. Choice of smoothing length used for Gaussian kernel may skew our estimate of β^*.
2. Non-linear contributions to velocities from nearby small scale structure may systematically bias results.
3. Triple valued regions may result in incorrectly reconstructed galaxy positions skewing velocity predictions derived therefrom.
4. As the reconstruction is being done in the LG frame, at each iteration we are subtracting the motion of the LG from all galaxies, our procedure may thus be susceptible to the Kaiser rocket effect.
5. Sparseness of survey may result in an under-representation of structures within the survey volume.
6. Structures which lie in the ZoA are not included in 2M++ and could contribute to the direction and amplitude of the motion of the LG as well as influencing predictions of peculiar velocities of galaxies near the galactic plane.
7. A non-linear relation between mass and luminosity as well as scatter in the underlying relation may influence predictions.

We have addressed some of these concerns above, but will review them again here for completeness.

In addressing (i), the width of the Gaussian kernel was chosen to be 4 h^{-1}Mpc as this length was shown to be least biased when velocity predictions were compared to those derived from simulations. Furthermore, this smoothing length was found to produce minimal scatter in the derived relation. We have accounted for (ii) and by performing the full reconstruction and analysis on data derived from N-body simulations. It was found that a value of 150 km s^{-1} should be used for the scatter around predictions to account for these effects. As for (iii), we used maximum likelihood methods to obtain our final result which integrate probabilities along the line-of-sight to account for triple valued regions. The value of β^* derived from this analysis was found to be unbiased when performed on simulations. A more complete discussion of the quantification of these systematics through analysis of N-body simulations can be found in Appendix A.

As seen from Figures 2.5 and 2.6 although the direction of the LG is not very susceptible to the value of β^*, the overall amplitude varies by 1,200 km s^{-1} between $\beta^*= 0$ and $\beta^*= 0.8$. As we are doing the reconstruction in the LG frame, an error in the estimate of the motion

of the reference frame may result in spurious distance estimates of objects along this line of motion. Putting objects at the incorrect distance may in turn result in incorrect object weights, and in turn, incorrect velocity predictions. This phenomenon has come to be known as the Kaiser "Rocket Effect", as it was first discussed in Kaiser (1988). To account for this effect Strauss et al. (1992) explored a "Kaiser Fix" to the IRAS 1.2 Jy sample. This "fix" amounts to altering the predicted distances of objects to

$$\begin{aligned} r = cz - \hat{\mathbf{r}} \cdot (\mathbf{V}(\mathbf{r}) - \mathbf{V}(\mathbf{0}) \exp(-r^2/r_{\rm K}^2) \\ - \mathbf{V}_{\rm CMB}[1 - \exp(-r^2/r_{\rm K}^2)]), \end{aligned} \tag{4.1}$$

where $\mathbf{V}_{\rm CMB}$ is the velocity of the LG as inferred from the CMB dipole, and where $r_{\rm K}$ is 1,000 km s^{-1}as determined by the observed velocity correlation function (Bertschinger et al., 1990). Note that this fix assumes that galaxies more distant than $r_{\rm K}$ are in fact at rest in the CMB frame, which may not be the case; indeed our data suggests otherwise. Nevertheless, to estimate the sensitivity of our results to this effect, we have implemented the Kaiser fix. We find that the final estimate of β^* differs by only 3%, which is small compared to the random errors.

The impact of survey sparseness on the methodology applied in this work has been estimated in the past by Pike & Hudson (2005). For the 2MASS catalogue they found that under-sampling by 50% produced negligible results on their final estimate of β^* (2-3%). Furthermore, we have accounted for the effects of sparse sampling by obtaining our quoted results and errors from bootstrap resampling of both 2M++ and peculiar velocity datasets. In addressing (vi) we measured β^* at high latitudes ($b > 50°$) and found no deviation from previous results beyond that of the random errors.

When the density field was normalized to the same bias, number-weighting and luminosity-weighting schemes yielded consistent results. As the χ^2 was found to be smaller for the luminosity weighted result than that obtained with number weighting, we hereafter will be quoting the best value of β^* as that obtained from the luminosity weighting scheme. Results obtained in this paper account for neither a non-linear relation between mass and luminosity, nor do they account for scatter in mass-luminosity relation. More sophisticated models have been proposed, such as the halo-model of Marinoni & Hudson (2002), and recently an iterative prescription to reconstruct the density field from the distribution of halos (Wang et al., 2009). We will consider implementation of such methods in a future paper.

4.3 Comparison With Other Results

As the bias is dependent on the relative abundance of galaxies of different morphology (*cf.* Pike & Hudson 2005), the value of β obtained is survey dependent. As 2M++ draws primarily from 2MASS, however, a loose comparison can be made with other values of β obtained therefrom. Most recently, in comparing the clustering dipole of galaxies

from 2MASS-XSC to predictions from linear theory assuming a ΛCDM cosmology and convergence of the LG dipole with that derived from the CMB, Bilicki et al. (2011) found $\beta = 0.38 \pm 0.04$. After constructing β dependent predictions of peculiar velocities, Branchini et al. (2012) in turn estimate β by minimizing the scatter of predicted 2MASS absolute magnitudes about a universal luminosity function and find $\beta = 0.323 \pm 0.083$. Davis et al. (2011) expand the velocity field in spherical harmonics and fit the inverse TF relation to SFI++ finding $\beta = 0.33 \pm 0.04$. These results are not consistent with the value of β found herein using a similar number-weighting scheme which is given approximately by $\beta^*/\psi^N_{\rm 2MRS}(32\,h^{-1}{\rm Mpc}) = 0.47 \pm 0.03$, where the distance used is the error-weighted depth of all individual SFI++ galaxies after the appropriate cuts on magnitude and velocity width discussed in Davis et al. (2011) above have been made.

Our value of $f\sigma_{8,\rm lin} = 0.40 \pm 0.02$ is in good agreement with those obtained using the same methodology, such as that of Turnbull et al. (2012) (0.40 ± 0.07), that of Pike & Hudson (2005) (0.44 ± 0.06), as well as with the weighted IRAS average of multiple studies reported therein (0.40 ± 0.03). It is, however, in tension with that found by Davis et al. (2011) (0.31 ± 0.04). Where necessary the values quoted here have been linearized following the procedure discussed above in §4.1.

4.4 Cosmological Implications

4.4.1 The value of $f\sigma_{8,\rm lin}$

We can also compare our value $f\sigma_{8,\rm lin}$to constraints placed on a degenerate combination of $\Omega_{\rm m}$ and σ_8 through independent means. For instance, analysis of second and third-order weak-lensing aperture-mass moments measured by CFHTLenS yield $\sigma_8(\Omega_{\rm m}/0.27)^{0.6} = 0.79 \pm 0.03$ (Kilbinger et al., 2013). Constraints can also be obtained from the number counts and mass of galaxy clusters as measured through X-ray surface brightness (Vikhlinin et al. 2009) and measurements of the Sunyaev-Zeldovich (SZ) effect (Planck Collaboration et al. 2013b, Reichardt et al. 2013). Finally, we can obtain a value for $f\sigma_8$ from CMB temperature anisotropy from Planck ($\Omega_{\rm m}^{0.55}\sigma_8 = 0.441 \pm 0.025$; Planck Collaboration et al., 2013a) and WMAP9 ($\Omega_{\rm m}^{0.55}\sigma_8 = 0.407 \pm 0.029$; Hinshaw et al., 2013). The measurements use different methods and are at different redshifts, and so their dependence on $\Omega_{\rm m}$ differs in the exponent. To make a qualitative comparisons between different results, we adopt $\Omega_{\rm m} = 0.3$ (see Figure 4.3). There is some tension between some results e.g. Kilbinger et al. (2013) and Planck SZ (Planck Collaboration et al., 2013b) versus Planck CMB temperature (Planck Collaboration et al., 2013a). The peculiar velocity result presented here is consistent with all of these values. Additionally, our value is consistent with the best-fit value of $f\sigma_8 = 0.40 \pm 0.02$ (Hudson & Turnbull 2012) obtained by combining measurements of $f(z)\sigma_8(z)$ at different redshifts through analysis of redshift space distortions.

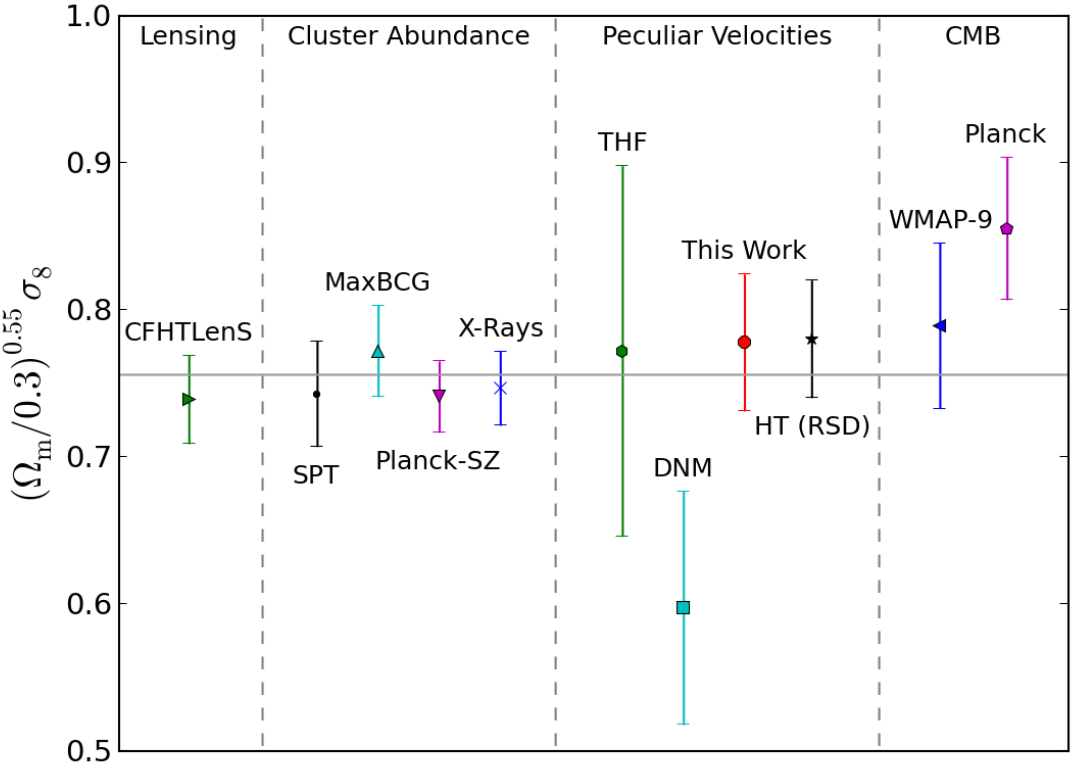

Figure 4.3: Comparison of $f\sigma_{8,\mathrm{lin}}$ measured results. Values plotted above that are derived from weak-lensing (Kilbinger et al. 2013, CFHTLenS) and cluster abundance (Reichardt et al. 2013 (SPT), Rozo et al. 2010 (MaxBCG), Planck Collaboration et al. 2013b (Planck-SZ), Vikhlinin et al. 2009 (X-rays)) have assumed a value of $\Omega_\mathrm{m} = 0.3$ in mapping constraints to $\Omega_\mathrm{m}^{0.55}\sigma_8$. Results obtained through analysis of measured velocities are also shown (Turnbull et al. 2012 (THF), Davis et al. 2011 (DNM)), as well as that obtained by combining constraints from redshift space distortions (Hudson & Turnbull 2012 (HT)). The horizontal line is the error-weighted mean of all values ($f\sigma_8 = 0.390 \pm 0.006$), shown here for reference only.

4.4.2 The motion of the LG

For our best value of β^* we can compare the predicted growth of the LG velocity amplitude with the result that one would expect to measure using linear theory for a ΛCDM cosmology (conditional on $V_{\rm CMB}$). For $\beta^* = 0.431 \pm 0.021$, as determined from peculiar velocity comparisons, we obtain the prediction for the motion of the Local Group arising from 2M++ to be 535 ± 40 km s^{-1}in the direction $l = 268^\circ \pm 4^\circ$, $b = 38^\circ \pm 6^\circ$, only 10° out of alignment with the direction of the motion as inferred from the CMB dipole. The residual LG motion is therefore 100 ± 37 km s^{-1}in the direction $l = 303^\circ \pm 36^\circ$, $b = 34^\circ \pm 36^\circ$. This value is in reasonable agreement with the best fit external obtained through peculiar velocity comparisons in the CMB frame of 159 ± 23 in the direction $l = 304^\circ \pm 11^\circ$, $b = 6^\circ \pm 13^\circ$. Inclusion of this dipole with the predicted motion of the LG arising from 2M++ results in a total predicted motion of 656 ± 47 km s^{-1} in the direction $l = 277^\circ \pm 4^\circ$, $b = 32^\circ \pm 6^\circ$, in even better agreement with both the amplitude and direction of the motion as inferred from the temperature dipole of the CMB.

4.4.3 The external dipole

Both the amplitude and direction of $\mathbf{V}_{\rm ext}$ that are preferred by each dataset, are consistent with one another. This suggests the value reported for $\mathbf{V}_{\rm ext}$ does not arise from a systematic effect in the measured velocities. Through comparing A1 with PSCz (of comparable depth to 2M++), Turnbull et al. (2012) similarly found a residual flow of $v_{\rm x} = 144 \pm 44$, $v_{\rm y} = -38 \pm 51$, $v_{\rm z} = 20 \pm 35$, in reasonable agreement with the values found here of $v_{\rm x} = 89 \pm 21$, $v_{\rm y} = -131 \pm 23$, $v_{\rm z} = 17 \pm 26$. This suggests that the dipole is not an artifact of either the analysis or redshift-catalogue, but is due to either a cosmographical or cosmological source. It is unclear, however, whether this dipole compensates for poor mapping between the density of galaxies and the mass of structures located beyond the majority of peculiar velocity data, or whether this dipole is sourced by structures beyond 2M++. A more sophisticated model for mapping luminosity to matter, such as abundance matching discussed earlier, will help to resolve this question.

It is worth noting that as the uncertainty weighted depth of all objects used is 32 h^{-1}Mpc, no matter the source of the dipole, therefore, the value for the derived bulk flow of a $50h^{-1}$Mpc sphere should remain largely unaffected. We compare the value for our determined amplitude of the bulk flow to that expected for a ΛCDM universe in Figure 4.4. We have plotted this comparison for the volume weighted average velocity arising from 2M++. It is apparent from this figure that the resulting bulk flow from our analysis is in agreement with that expected for a ΛCDM Universe. Combining the cosmic variance in quadrature with observational errors, comparison of the measured bulk flow of a 200 h^{-1}Mpc sphere with predictions from ΛCDM yield a χ^2 of 0.7; clearly the measured value agrees well with the prediction from ΛCDM.

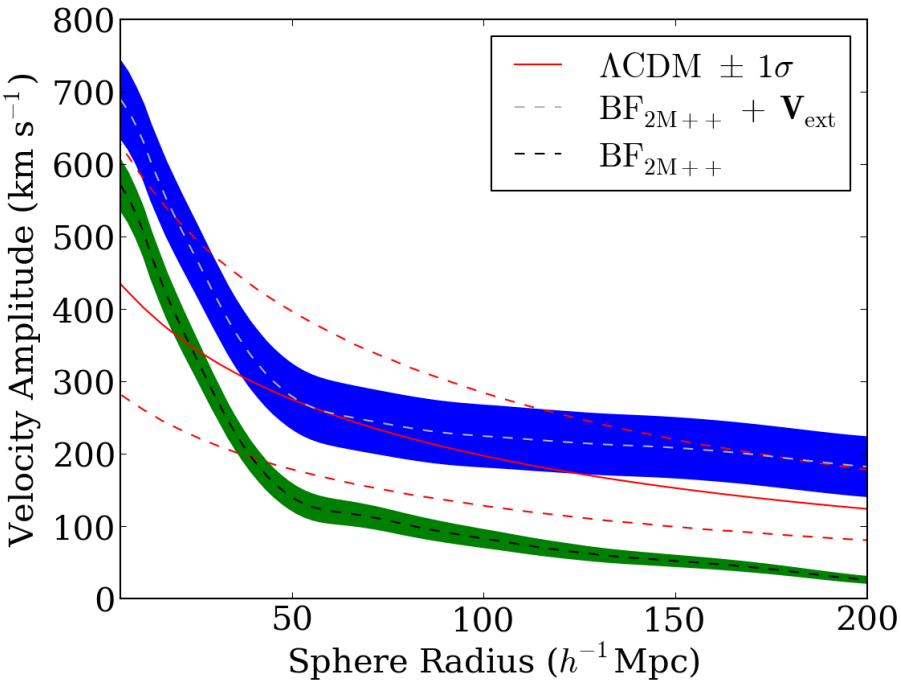

Figure 4.4: Predicted amplitude of mean velocity of a top-hat sphere centered on the LG as a function of sphere radius. The predicted root-mean-square velocity for a ΛCDM cosmology is shown as the red solid line, the cosmic scatter in the velocity amplitude distribution are shown as red dashed lines. All errors plotted are 1σ.

4.4.4 A large-scale underdensity?

There have been recent claims that the Local Universe ($\sim$150 h^{-1}Mpc) is observed to be under-dense (Whitbourn & Shanks 2013, Keenan et al. 2013). Such a phenomenon might account for the discrepancy between the larger value for the Hubble parameter when measured locally ($z \approx 0$) and that obtained from studies of the CMB temperature anisotropies. Although the majority of 2M++ lies within the suggested under-density, we have nonetheless explored the possibility of a under-dense volume *within* 2M++. The luminosity-weighted density contrast of 2M++ is shown in Figure 4.5. We have not observed any systematic rise in density towards the periphery of the survey.

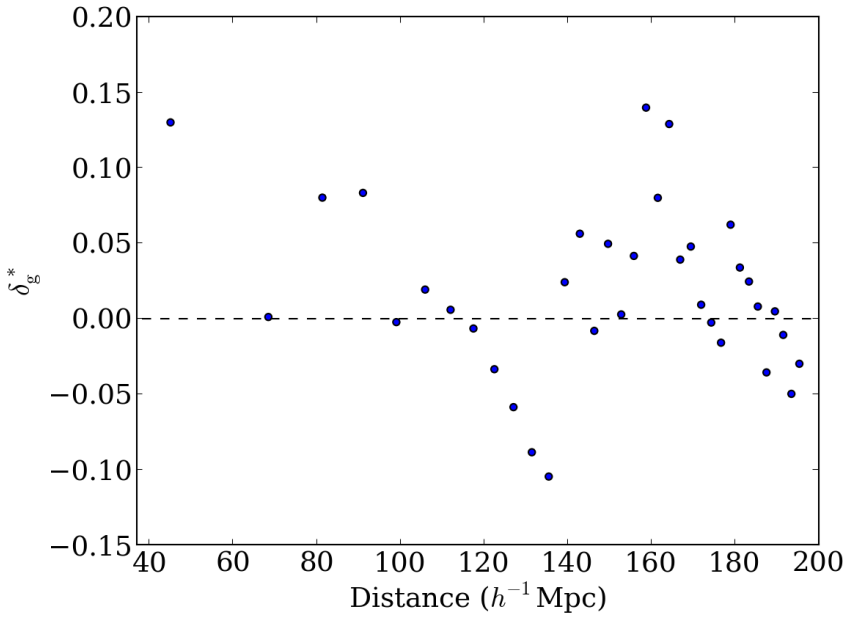

Figure 4.5: The mean density contrast of concentric spherical shells of equal volume centered on the Local Group.

Chapter 5

Conclusions

5.1 Summary

Under the assumption of gravitational instability we utilized linear theory to iteratively reconstruct the density field within 200 h^{-1}Mpc from 2M++, a composite all-sky redshift redshift survey with high completeness. We compared the predicted velocities arising from this density field to the measured peculiar velocities of SFI++ and the First Amendment supernovae dataset using various comparison methods in order to measure $\beta^* = \Omega_{\rm m}^{0.55}/b^*$. Using the VELMOD maximum likelihood comparison method with SFI++ spiral galaxies we simultaneously solved for the inverse TF relation zeropoint and slope, β^*, as well as an external dipole denoted $\mathbf{V}_{\rm ext}$. We similarily compared peculiar velocities datasets to predictions from 2M++ using a forward-likelihood method in order to constrain β^* and $\mathbf{V}_{\rm ext}$. All methods and data subsets yielded consistent values, with our final result being β^* = 0.431 ± 0.021. Combining this value of β^* with $\sigma^*_{8,\rm gal} = 0.990 \pm 0.035$ as measured from 2M++ for the preferred value of β^* quoted above, we in turn measured the parameter combination $f\sigma_{8,\rm lin}$ = 0.401 ± 0.024. This value was found to be consistent with the majority of results obtained by independent means, including those of WMAP9 and Planck.

For our measured value of β^* we computed the velocity of the Local Group as predicted by linear theory arising from the reconstructed density field. Our value for the velocity was found to be consistent with the theoretical value that would be measured for a survey of this depth in a ΛCDM Universe. Combining our predicted motion of LG arising from 2M++ for our best value of β^* with the value of $\mathbf{V}_{\rm ext}$ obtained through comparing predicted velocities with mesured velocities, we predict the total motion of the LG to be 660 ± 50 km s^{-1}, towards $l = 277^\circ \pm 4^\circ$, $b = 32^\circ \pm 6^\circ$, only 5° out of alignment with the direction as inferred from the CMB dipole. Similarly, with addition of this dipole to the 50 h^{-1}Mpc Gaussian weighted mean of the velocity field, we obtain a predicted bulk-flow of 230 ± 30 km s^{-1}, towards $l = 293^\circ \pm 8^\circ$, $b = 14^\circ \pm 10^\circ$, an amplitude that is consistent with that expected for a ΛCDM Universe. We note, however, that although we find the inclusion of $\mathbf{V}_{\rm ext}$ is preferred at the 5.1σ level, it is unclear whether this dipole merely compensates for

poor mapping between luminosity and mass towards the periphery of 2M++, or whether it accounts for structures beyond the 2M++. Future work using more sophisticated biasing schemes are required to resolve this issue. For preliminary results using an abundance matching scheme to map brightest cluster galaxies to halo mass see Appendix B.

5.2 Future Directions

In the context of velocity-velocity comparisons discussed in this work, the future of PVs seems bright. There are several upcoming peculiar velocity surveys which should dramatically improve the constraints on both β^* and $f\sigma_8$. The 6dF Galaxy Redshift Survey (6dFGRS), for instance, is a combined redshift and peculiar velocity survey of the southern hemisphere covering latitudes $b > 10°$, out to a depth of $z \sim 0.15$. It has most recently acquired ∼125,000 redshifts, ∼8,900 of which have fundamental plane (FP) derived distances within $z \sim 0.055$ (Campbell et al., 2014). SDSS has recently acquired FP distance measurements that include a sample of ∼93,000 ellipticals out to $z < 0.2$ (Saulder et al., 2013), with additional data releases expected in the near future. Other upcoming surveys include the Transforming Astronomical Imaging surveys through Polychromatic Analysis of Nebulae (TAIPAN) survey. Using the UK Schmidt telescope, it is estimated that TAIPAN will acquire ∼45,000 Fundamental-Plane velocity measurements out to a redshift of 0.2 (Koda et al. 2013). The next generation of Tully-Fisher (TF) peculiar velocity surveys include the Widefield ASKAP L-band Legacy All-sky Blind surveY (WALLABY, Koribalski & Staveley-Smith 2009), and the Westerbork Northern Sky HI Survey (WNSHS). An HI survey acquired using the Australian Square Kilometer Array Pathfinder (ASKAP), WALLABY is planned to cover 3π steradian of sky. Its Northern Hemisphere counterpart, WNSHS, is planned to cover remaining π steradian of the sky using the Westerbork Synthesis Radio. It is estimated that these surveys will obtain a total of ∼32,000 velocity measurements, and along with TAIPAN will not only enable k-dependent measurements of $f\sigma_8$ but will improve constraints on this parameter combination at low-redshift ($z \leq 0.05$) to within 3% (Koda et al. 2013).

It is important to consider, however, the general limitations of the approach taken in this work. Peculiar velocity measurements used in this analysis were derived from galaxy distance measurements. As the errors in such measurements are proportional to distance, they are limited to probing scales smaller than ∼100 h^{-1}Mpc. In order to constrain the power spectrum of mass fluctuations on larger physical scales (*e.g.* 100-1000 h^{-1}Mpc), alternative methods for measuring peculiar velocities are required. One such method is through the kinetic Sunyaev-Zel'dovich effect (kSZ, Sunyaev & Zeldovich 1980), in which the bulk motion (relative to the CMB) of ionized gas in clusters (Kashlinsky & Atrio-Barandela, 2000) or galaxy halos (Lavaux et al., 2013) can be detected through scattering of CMB photons. As the errors in measured velocities derived from this effect are independent of distance, prospects for measuring large-scale flows from kSZ may prove more promising.

References

Aaronson M., Huchra J., Mould J., Schechter P. L., Tully R. B., 1982, ApJ, 258, 64

Abazajian K. N. et al., 2009, ApJS, 182, 543

Afshordi N., Loh Y.-S., Strauss M. A., 2004, PhRvD, 69, 083524

Bardeen J. M., Bond J. R., Kaiser N., Szalay A. S., 1986, ApJ, 304, 15

Barnes T. G., 2009, in American Institute of Physics Conference Series, Vol. 1170, American Institute of Physics Conference Series, Guzik J. A., Bradley P. A., eds., pp. 3–12

Behroozi P. S., Wechsler R. H., Wu H.-Y., 2013, ApJ, 762, 109

Berlind A. A., Narayanan V. K., Weinberg D. H., 2000, ApJ, 537, 537

Bertschinger E., Gorski K. M., Dekel A., 1990, Nature, 345, 507

Bilicki M., Chodorowski M., Hellwing W., Jarrett T., Mamon G., 2012, ArXiv e-prints

Bilicki M., Chodorowski M., Jarrett T., Mamon G. A., 2011, ApJ, 741, 31

Bilicki M., Chodorowski M., Mamon G. A., Jarrett T., 2011, ApJ, 741, 31

Blanton M. R. et al., 2005, AJ, 129, 2562

Bond J. R., Efstathiou G., 1984, ApJL, 285, L45

Branchini E., Davis M., Nusser A., 2012, MNRAS, 424, 472

Burstein D., Faber S. M., Dressler A., 1990, ApJ, 354, 18

Campbell L. A. et al., 2014, ArXiv e-prints

Colin J., Mohayaee R., Sarkar S., Shafieloo A., 2011, MNRAS, 414, 264

Conklin E. K., 1969, Nature, 222, 971

Dai D.-C., Kinney W. H., Stojkovic D., 2011, JCAP, 4, 15

Davis M., Huchra J., 1982, ApJ, 254, 437

Davis M., Nusser A., Masters K. L., Springob C., Huchra J. P., Lemson G., 2011, MNRAS, 413, 2906

de Bernardis P. et al., 2000, Nature, 404, 955

de Vaucouleurs G., Peters W. L., 1981, ApJ, 248, 395

Dekel A., Lahav O., 1999, ApJ 520

Dressler A., 1988, ApJ, 329, 519

Dressler A., Faber S. M., 1990, ApJ, 354, 13

Dressler A., Faber S. M., Burstein D., Davies R. L., Lynden-Bell D., Terlevich R. J., Wegner G., 1987, ApJL, 313, L37

Efstathiou G., Kaiser N., Saunders W., Lawrence A., Rowan-Robinson M., Ellis R. S., Frenk C. S., 1990a, MNRAS, 247, 10P

Efstathiou G., Sutherland W. J., Maddox S. J., 1990b, Nature, 348, 705

Einasto J., Kaasik A., Saar E., 1974, Tartu Astrofüüs. Obs. Preprint, Nr. 1, 8 p., 1, 3

Einstein A., 1917, Sitzungsberichte der Königlich Preußischen Akademie der Wissenschaften (Berlin), Seite 142-152., 142

Erdogdu P. et al., 2006, MNRAS, 368, 1515

Erdoğdu P. et al., 2006, MNRAS, 373, 45

Folatelli G., Phillips M. M., Burns C. R., Contreras C., 2010, AJ, 139, 120

Freedman W. L., Madore B. F., 2010, ARA&A, 48, 673

Gamow G., 1946, Physical Review, 70, 572

Giovanelli R., Haynes M. P., Herter T., Vogt N. P., da Costa L. N., Freudling W., Salzer J. J., Wegner G., 1997, AJ, 113, 53

Hicken M., Wood-Vasey W. M., Blondin S., Challis P., Jha S., Kelly P. L., Rest A., Kirshner R. P., 2009, ApJ, 700, 1097

Hinshaw G. et al., 2013, ApJS, 208, 19

Hubble E., 1929, Proceedings of the National Academy of Science, 15, 168

Huchra J. P., Geller M. J., 1982, ApJ, 257, 423

Huchra J. P. et al., 2012, ApJS, 199, 26

Hudson M. J., 1993, MNRAS, 265, 43

Hudson M. J., 1994a, MNRAS, 266, 475

Hudson M. J., 1994b, MNRAS, 266, 468

Hudson M. J., Turnbull S. J., 2012, ApJL, 751, L30

Jha S., Riess A. G., Kirshner R. P., 2007, ApJ, 659, 122

Jones D. H. et al., 2009, MNRAS, 399, 683

Juszkiewicz R., Feldman H. A., Fry J. N., Jaffe A. H., 2010, JCAP, 2, 21

Kaiser N., 1984, ApJL, 284, L9

Kaiser N., 1988, MNRAS, 231, 149

Kashlinsky A., Atrio-Barandela F., 2000, ApJL, 536, L67

Kashlinsky A., Atrio-Barandela F., Kocevski D., Ebeling H., 2008, ApJL, 686, L49

Keenan R. C., Barger A. J., Cowie L. L., 2013, ApJ, 775, 62

Kilbinger M., Fu L., Heymans C., Simpson F., Benjamin J., Erben T., Harnois-Deraps, 2013, MNRAS, 430, 735

Klypin A. A., Trujillo-Gomez S., Primack J., 2011, ApJ, 740, 102

Kocevski D. D., Ebeling H., 2006, ApJ, 645, 1043

Koda J. et al., 2013, ArXiv e-prints

Kogut A. et al., 1993, ApJ, 419, 1

Koribalski B., Staveley-Smith L., 2009, ASKAP Survey Science Proposal

Lahav O., Kaiser N., Hoffman Y., 1990, ApJ, 352, 448

Lavaux G., Afshordi N., Hudson M. J., 2013, MNRAS, 430, 1617

Lavaux G., Hudson M. J., 2011, MNRAS, 416, 2840

Lavaux G., Tully R. B., Mohayaee R., Colombi S., 2010, ApJ, 709, 483

Leavitt H. S., 1908, Annals of Harvard College Observatory, 60, 87

Lilje P. B., Yahil A., Jones B. J. T., 1986, ApJ, 307, 91

Lineweaver C. H., 1997, in Microwave Background Anisotropies, Bouchet F. R., Gispert R., Guiderdoni B., Trân Thanh Vân J., eds., pp. 69–75

Lynden-Bell D., Faber S. M., Burstein D., Davies R. L., Dressler A., Terlevich R. J., Wegner G., 1988, ApJ, 326, 19

Maddox S. J., Efstathiou G., Sutherland W. J., Loveday J., 1990, MNRAS, 242, 43P

Marinoni C., Hudson M. J., 2002, ApJ, 569, 101

Masters K. L., Springob C. M., Haynes M. P., Giovanelli R., 2006, ApJ, 653, 861

Mathewson D. S., Ford V. L., 1994, ApJL, 434, L39

Mo H., van den Bosch F., White S., 2011, Galaxy Formation and Evolution. Cambridge University Press

Norberg P. et al., 2001, MNRAS, 328, 64

Nusser A., Davis M., 1995, MNRAS, 276, 1391

Nusser A., Davis M., 2011, ApJ, 736, 93

Oort J. H., 1940, ApJ, 91, 273

Ostriker J. P., Peebles P. J. E., Yahil A., 1974, ApJL, 193, L1

Penzias A. A., Wilson R. W., 1965, ApJ, 142, 419

Perlmutter S. et al., 1999, ApJ, 517, 565

Phillips M. M., 1993, ApJL, 413, L105

Pike R. W., Hudson M. J., 2005, ApJ, 635, 11

Planck Collaboration et al., 2013a, ArXiv e-prints

Planck Collaboration et al., 2013b, ArXiv e-prints

Planck Collaboration et al., 2013c, ArXiv e-prints

Press W. H., Schechter P., 1974, ApJ, 187, 425

Reichardt C. L. et al., 2013, ApJ, 763, 127

Riess A. G. et al., 1998, AJ, 116, 1009

Riess A. G. et al., 2009, ApJS, 183, 109

Rozo E. et al., 2010, ApJ, 708, 645

Sakai S., Mould J. R., Huchra J. P., Hughes S., Macri L. M., Kennicutt, Jr. R. C., 2000, in Astronomical Society of the Pacific Conference Series, Vol. 201, Cosmic Flows Workshop, Courteau S., Willick J., eds., p. 129

Saulder C., Mieske S., Zeilinger W. W., Chilingarian I., 2013, A&A, 557, A21

Saunders W. et al., 2000, MNRAS, 317, 55

Schechter P., 1976, ApJ, 203, 297

Schechter P. L., 1980, AJ, 85, 801

Skrutskie M. F. et al., 2006, AJ, 131, 1163

Slipher V. M., 1917, Proceedings of the American Philosophical Society, 56, 403

Springel V., 2005, MNRAS, 364, 1105

Springob C. M., Masters K. L., Haynes M. P., Giovanelli R., Marinoni C., 2007, ApJS, 172, 599

Strauss M. A., 1989, PhD thesis, California Univ., Berkeley.

Strauss M. A., Davis M., 1988, The peculiar velocity field predicted by the distribution of IRAS galaxies. pp. 255–274

Strauss M. A., Yahil A., Davis M., Huchra J. P., Fisher K., 1992, ApJ, 397, 395

Sunyaev R. A., Zeldovich I. B., 1980, MNRAS, 190, 413

Tegmark M., Dodelson S., Eisenstein D. J., Narayanan V., 2002, ApJ, 571, 191

Tully R. B., Fisher J. R., 1977, A&A, 54, 661

Tully R. B., Pierce M. J., 2000, ApJ, 533, 744

Turnbull S. J., Hudson M. J., Feldman H. A., Hicken M., Kirshner R. P., Watkins R., 2012, MNRAS, 420, 447

Vikhlinin A. et al., 2009, ApJ, 692, 1060

Vittorio N., Juszkiewicz R., Davis M., 1986, Nature, 323, 132

Wang H., Mo H. J., Jing Y. P., Guo Y., van den Bosch F. C., Yang X., 2009, MNRAS, 394, 398

Wang L., Steinhardt P. J., 1998, ApJ, 508, 483

Watkins R., Feldman H. A., Hudson M. J., 2009, MNRAS, 392, 743

Westover M., 2007, PhD dissertation, Harvard University, Department of Astronomy

Whelan J., Iben, Jr. I., 1973, ApJ, 186, 1007

Whitbourn J. R., Shanks T., 2013, MNRAS

Willick J. A., Strauss M. A., 1998, ApJ, 507, 64

Willick J. A., Strauss M. A., Dekel A., Kolatt T., 1997, ApJ, 486, 629

Yahil A., Sandage A., Tammann G. A., 1980, PhySc, 21, 635

Yahil A., Strauss M. A., Davis M., Huchra J. P., 1991a, ApJ, 372, 380

Yahil A., Strauss M. A., Davis M., Huchra J. P., 1991b, ApJ, 372, 380

Zwicky F., 1933, Helvetica Physica Acta, 6, 110

Appendix A

Results From N-Body Simulation

The original text and figures which comprise this appendix were produced by Stephen Turnbull. Results discussed in §A.1.1, however, were produced independently by this author.

A.1 Tests of the Reconstruction with N-body Simulations

In this appendix, we focus on two possible sources of systematic bias in the reconstructed density and velocity fields. First, when constructing the density field from a set of point density tracers, it is necessary to smooth to obtain a continuous density field. If the smoothing length is too short, density contrasts are high and linear theory is no longer applicable. If the smoothing length is too long, then the density contrast is suppressed and velocities are underpredicted. Second, in "reconstructing" real-space positions from redshift-space, the iterative technique discussed in §2.5 may also introduce a systematic bias in the recovered density field and hence in the fitted value of β.

A.1.1 Effect of smoothing

Berlind et al. (2000) used N-body simulations to show that when predicted velocities derived from smooth density fields are compared to measured (unsmoothed) velocities, the recovered value of β depends on the smoothing. For Gaussian smoothing, unbiased results were obtained for a smoothing radius between 4 and 5 h^{-1}Mpc. It is interesting to confirm these results.

Here we use an N-body simulation of 512^3 particles in a 500 h^{-1} Mpc periodic box using GADGET-2 (Springel 2005). The cosmological parameters of this simulation are as follows: $\Omega_m = 0.266$, $\Omega_\Lambda = 0.734$, $h = 0.71$, and where each particle is $6.83 \times 10^{10}\ h^{-1} M_\odot$.

From the particle positions and velocities of the simulation a halo catalog was formed using ROCKSTAR (Behroozi et al. 2013) consisting of 693,948 halos between 5.5×10^{11} and 2.2×10^{15} h^{-1} $M_{\odot}$ (between 8 and 31809 particles). Either halo or particle positions were smoothed to create a smooth halo or particle density field.

In Fig. A.1 we plot both the slope of regression between smoothed predicted and N-body velocities, as well as the scatter about this relation, both as a function of smoothing scale.

For particle velocities compared with linear theory predictions from the smoothed particle density field, the slope is unbiased at a smoothing scale of $\sim$5 h^{-1}Mpc. The scatter is $\sim$250 km s^{-1}. The results are similar for halos, but the scatter is significantly lower: $\sim$150 km s^{-1}. This is because the particle velocity field is a sum of the motion of the haloes themselves plus the internal motion of particles with respect to the haloes. In both cases, the scatter is minimum for a smoothing scale of $\sim$4 h^{-1}Mpc.

A.1.2 Reconstructing the Halo Distances from Redshifts

With actual galaxy data, the true distances are unknown but redshifts are available. In this paper, we use an iterative reconstruction method to map a galaxy's position from redshift space to real space. We will refer to these reconstructed coordinates as "recon-space." In the N-body simulation, we emulate this by placing halos in redshift-space, and then iteratively reconstruct the density field, slowly increasing β.

Fig. A.2 shows the difference between real-space positions and recon-space positions. The left panel illustrates the absolute displacement in units of km s^{-1}. From this panel, it is apparent that in recon-space the majority of haloes do in fact return to a location close to their real-space positions, with an error that is typically $\sim$ 300 km s^{-1}. This is smaller than the smoothing scale of $\sim 4h^{-1}$ Mpc. However, in practice this reconstruction error will act as an additional source of smoothing. We will return to this point below.

The right panel shows the displacement of each halo from its real-space position normalized by the difference between the real-space and redshift-space positions (*i.e.* by their peculiar velocities). In this way the halos which lie in redshift-space have a normalized displacement of -1, and those which have returned to real-space have a normalized displacement of 0. With each successive iteration tracers would all ideally return to 0, *i.e.* return to the position they had in real-space. Halos which have a normalized displacement more negative than -1 have moved away from their initial positions. We argue below (§A.2) that these are haloes in triple-valued regions. From this figure it can be seen that the typical tracer does in fact return to its real-space position. However, the distinction between low and high peculiar velocity tracers is more pronounced. The tracers with a low peculiar velocity have a symmetric distribution of reconstruction error. The halos which initially have a high velocity, however, have a more skewed distribution which likely results in part from triple-valued regions.

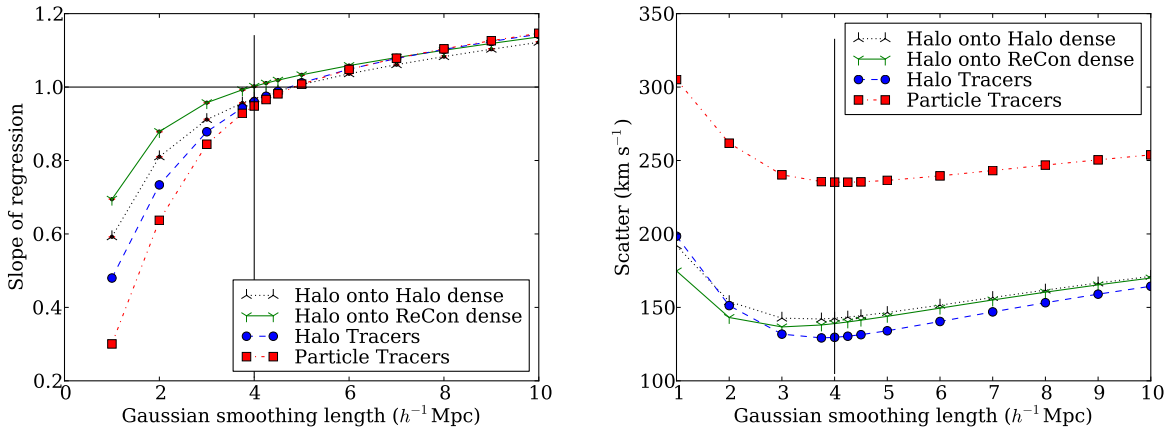

Figure A.1: The fitted slope of the regression between N-body observed peculiar velocities and the linear theory predictions as a function of smoothing scale is shown in the left panel. In the right panel the scatter about the same regression is plotted. Either particles or halos can be used as tracers of the density field, or as tracers of the velocity field. The blue circles and red squares represent halo tracers and particle tracers, respectively. The black curve with downwards pointing 'Y' show the resulting scatter when the known halo velocities are compared to the predictions from the halo density field. The green curve with 'Y'-shaped symbols show the resulting scatter when the known halo velocities are compared to the predictions from the reconstructed halo density field. Note that the reconstruction process shows very nearly unbiased results when the field is smoothed with a Gaussian kernel that is 4 h^{-1}Mpc in length.

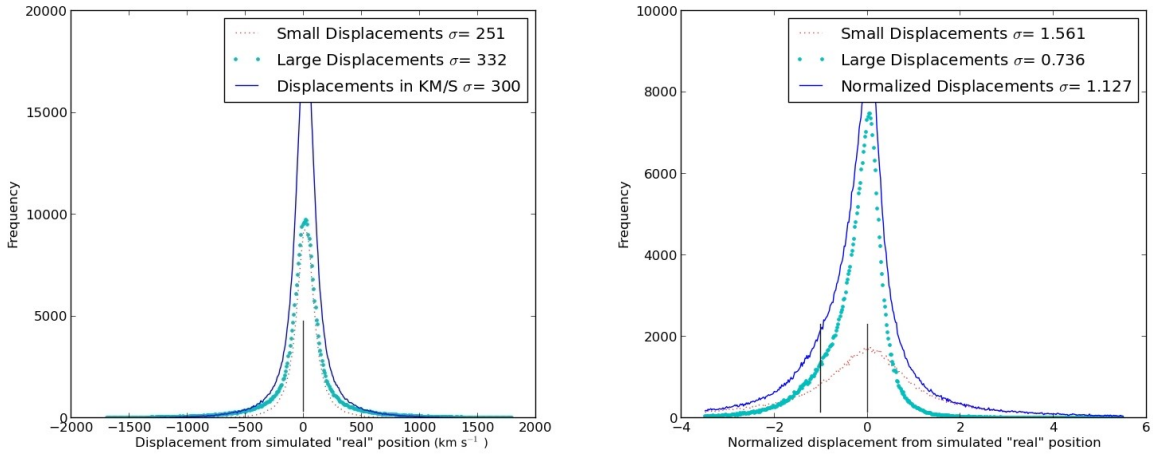

Figure A.2: Two sample histograms showing the relative displacement of halos in recon-space to their real-space positions. The recon-space positions used are those which correspond to the number of iterations required to recover the known value of β. The left panel illustrates the absolute displacement in km s^{-1}, whereas the right panel shows the displacement of halos normalized by the difference between real-space and redshift-space positions. As such, a normalized displacement of -1 corresponds to a halo lying at its redshift-space position, and a normalized displacement of 0 corresponds to a halo returning to its real-space position. The solid blue curve corresponds to all halos, the turquoise dotted curve corresponds to halos with known velocities greater than 150 km s^{-1}, and the dotted red curve corresponds to halos with known velocities less than 150 km s^{-1}. Halos which have a normalized displacement less than -1 have moved away from their initial positions due to lying within triple-valued regions. Halos which have a normalized displacement greater than 0 have moved to their initial positions and beyond.

Having reconstructed the density field in recon-space, we return to the question of how well this field, once smoothed, can predict peculiar velocities. Fig. A.1 shows the results of this comparison. The fitted slope obtained from the reconstructed density field is systematically offset in comparison to those obtained from the real-space halo density field. The key result is that predicted velocities derived from the reconstructed smoothed halo fields yields an unbiased value of the slope, *i.e.* β, when a Gaussian kernel of 4 h^{-1}Mpc is used. This value is smaller than the value of $\sim$5 h^{-1}Mpc found for haloes in real-space, because the recon-space density field is effectively pre-smoothed (in the redshift direction) by the $\sim$ 300 km s^{-1} reconstruction error discussed above.

A.2 Iterative Reconstruction Near Triple-Valued Regions

One problem with any reconstruction method is correcting for the fact that mapping from redshift to position is multivalued, *i.e.* there can be several distances which map to the same redshift.

To give an illustration as to how triple-valued-regions affects the iterative reconstruction method, we have created a simple toy model in Fig. A.3 which shows the velocity field around a spherical overdensity. One can see that for any object with an observed redshift in the range $\sim$ 100 to $\sim$ 300 km s^{-1}, there are multiple distances that correspond to that given redshift. As a concrete example, consider a galaxy at a redshift of 300 km s^{-1}. We will consider a simplified version of our reconstruction scheme in order to illustrate the general behaviour. In this simplified version, the value of β is held fixed, i.e. it is not increased adiabatically, so the amplitude of the peculiar velocity curve is fixed and the curve $cz(r)$ is also fixed.

In the first step of this iterative process, we place the galaxy at a distance corresponding to its observed redshift: 300 km s^{-1} (position 1). At this location the predicted peculiar velocity is approximately -190 km s^{-1} , so the object is moved to its first reconstructed position of 490 km s^{-1} = 300 km s^{-1} $-$ ($-$190 km s^{-1}) (position 2). At this position it has a predicted peculiar velocity of approximately $-$20 km s^{-1}, and so this predicted peculiar velocity is again subtracted from its observed redshift of 300 km s^{-1}, resulting in a reconstructed distance of 320 km s^{-1} (position 3). In this example, each successive loop brings the reconstructed position closer to the outer redshift solution of approximately 360 km s^{-1}. The same behaviour occurs for redshifts between 250 and 400 km s^{-1}, the final position converges to the third (outer) of the three values. For redshifts between 100 and 250 km s^{-1}, in contrast, the recon position converges to the first of the three values. One can see that the outer solutions are attractors, and the middle solution is unstable.

The above toy model is for a test particle (*e.g.* galaxy) moving in a fixed potential well (*e.g.* sueprcluster). It can also happen that two similar-mass galaxies (or two clusters) may each respond to the other's gravity. In this situation, the distances of the two objects can

"leapfrog", *i.e.* can exchange the order of their distances in reconstructed space. This leads to a sign change of the predicted peculiar velocity, which the leads to another "leapfrog" and a subsequent sign change in predicted peculiar velocity. Hence some objects show oscillatory behaviour in the reconstructed distance.

Note however that the simple model described above and in Fig. A.3 is an over-simplification of our reconstruction process. Of course, while in reality the density field used is a smoothed Gaussian random sphere not a spherical top-hat overdensity, qualitatively the behaviour around overdensities is similar. More importantly, our iterative scheme is more complex than the one outlined above. First, we "adiabatically" increase β^* at each iteration. Consequently, the amplitude of the predicted peculiar velocity field increase slowly and so the size of triple-valued regions in redshifts space grows slowly. Second, we reduce oscillatory behaviour by averaging the positions of several successive iterations. Thus the convergence is better-behaved than the toy model described above. But qualitatively, the effect remains the same: as a result of preferentially placing objects towards the periphery of triple-value regions, the density field is effectively "smoothed" more in the regions of highest density.

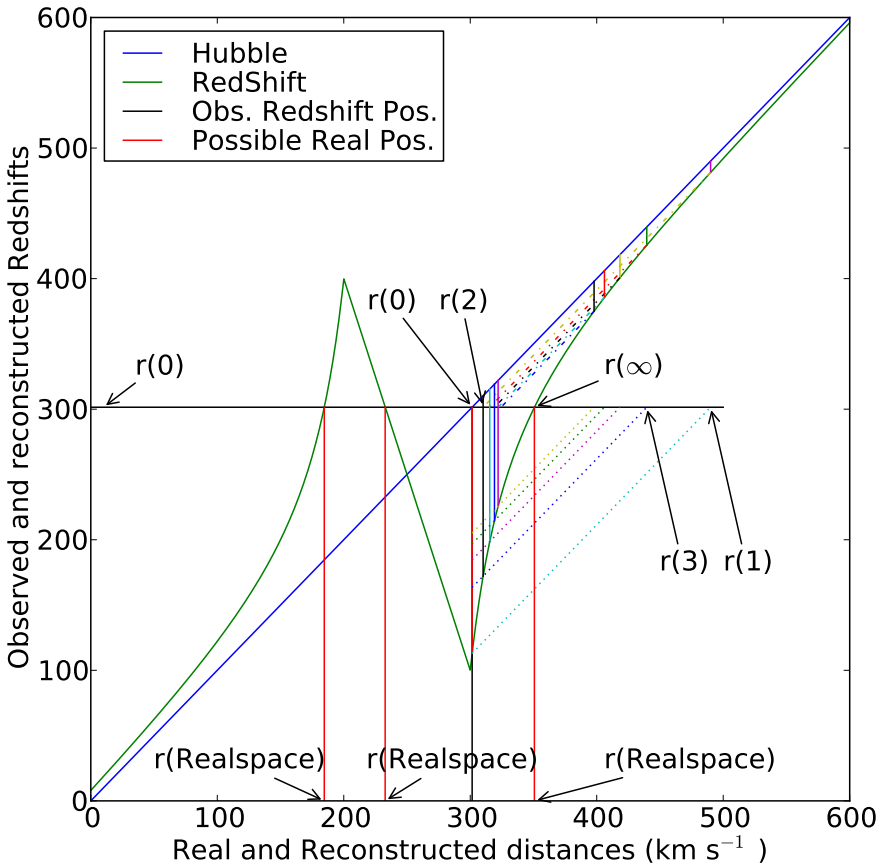

Figure A.3: Simplified reconstruction of one test object near a fixed potential well. In a Universe without structure, Hubble's law (blue solid line $y = x$) would be sufficient to convert from redshift to real-space positions. In a Universe containing a spherical top-hat overdensity, however, the relation is complicated by infall towards the well (green solid curve). An object with an observed redshift in excess of 300 km s^{-1} can be seen to have originated from three possible real-space positions (vertical red solid lines). The reconstruction process starts by placing the particle at it's observed redshift, predicting its velocity, and then subtracting that prediction from the original observation (the dotted lines parallel to the Hubble law line) to get a new predicted position. In most situations this new position will be beyond one of the possible real-space positions where the predicted infall velocities are small. Repeating the process here results in a much smaller velocity offset which can be projected (dot-dashed lines) back to the observed velocity to find the next reconstructed position. The iterative reconstruction converges in most situations to one of the two outer possible real-space positions. Reconstructed positions never converge, however, to the central possible real-space position.

Appendix B

Mass Weighting Through Abundance Matching

Throughout this work we have assumed that either all galaxies have the same halo mass irrespective of their properties (in the case of a number weighting scheme), or that the luminosity of a galaxy is directly proportional to the mass of its halo (in the case of luminosity weighting). Both schemes are naive, and in this appendix we consider a more sophisticated means of estimating halo mass from galaxy luminosity. We explore implementation of a technique referred to as "Abundance Matching" first suggested by Marinoni & Hudson (2002), in which the mass function predicted by Press-Schecter formalism (Press & Schechter, 1974) is compared to an observationally derived luminosity function to yield predictions for a luminosity dependent mass-to-light ratio. Using brightest cluster galaxies (BGCs) from 2M++ we apply this methodology in an attempt to map the luminosity of these objects to the mass of their dark halos. We stress that results reported here are preliminary, and as such, should be scrutinized accordingly.

B.1 Abundance Matching

B.1.1 Overview

Abundance matching requires assuming a monotonic and deterministic relationship between a system's luminosity and mass, or in this case, between the intrinsic luminosity of a BCG and the mass of its halo. The existence of such a relation implies that the number density of objects with luminosity greater than L_s is equal to the number density of objects above a mass $M_s = f(L_s)$, where $f(L)$ is our deterministic mapping from luminosity to mass. In the event that the system is well described by a luminosity function, $\phi(L)$, (*e.g.* Schechter luminosity function; Schechter 1976), the number density of objects above luminosity L_s would then be given by

$$N(> L_s) = \int_{L_s}^{\infty} \phi(L) dL. \tag{B.1}$$

For a corresponding differential halo mass function, $\phi(\mathcal{M})$, (*e.g.* from Press-Schechter formalism), the mass of an object of luminosity L_s can then be obtained from

$$N(> \mathcal{M}_s) = N(> L_s) \iff \int_{\mathcal{M}_s}^{\infty} \phi(\mathcal{M})\, d\mathcal{M} = \int_{L_s}^{\infty} \phi(L) dL. \tag{B.2}$$

B.1.2 Implementation

The differential mass function used in this analysis was derived from the Bolshoi simulation of Klypin et al. (2011). This simulation uses 2048^3 particles, has high mass resolution ($1.35 \times 10^8\ h^{-1}\mathrm{M}_\odot$), high force resolution ($1\ h^{-1}$kpc) and is of comparable size to 2M++ ($250\ h^{-1}$Mpc). The differential mass function derived from this catalogue was found to be well modeled by

$$\phi(\mathcal{M}) = \phi^* \left(\frac{\mathcal{M}}{\mathcal{M}^*}\right)^{\alpha} e^{-\mathcal{M}/\mathcal{M}^*}, \tag{B.3}$$

for $\alpha = -1.98$, $\mathcal{M}^* = 10^{14.6}\ h^{-1} M_\odot$, and $\phi^* = 10^{-5.6}$, and is shown in Figure B.1.

The brightest cluster galaxies from 2M++ were identified by first grouping the galaxies using the "Friends-of-friends" algorithm of Huchra & Geller (1982), and then extracting the brightest galaxies from all groups (including "groups" of 1 galaxy). The number density within magnitude bins of width 0.25 Mag were then obtained from BCG counts within volume limited subsets of 2M++ (see Figure B.1). These measurements were not modelled with a functional form, however, but were instead used directly in Equation (B.2) in combination with the functional form for the differential mass function of Equation (B.3). Results from this analysis are shown in Figure B.2.

From Figure B.2 it is observed that the mass-to-light ratio (Υ) decreases as $\Upsilon \sim L^{-0.5}$ to a minimum at a luminosity of $\sim 3 \times 10^{10}\ h^{-2} L_\odot$ ($\Upsilon \sim 40\ h \Upsilon_\odot$), and rises steeply thereafter ($\Upsilon \sim L^3$).

B.2 Density Field Reconstruction

Using the relations found above we here consider modifications to the density field reconstruction methodology discussed in Chapter 2. Firstly, in order to normalize the density contrast to the bias of an L^* galaxy, we must determine the mean mass weighted bias as a function of distance, *i.e.*

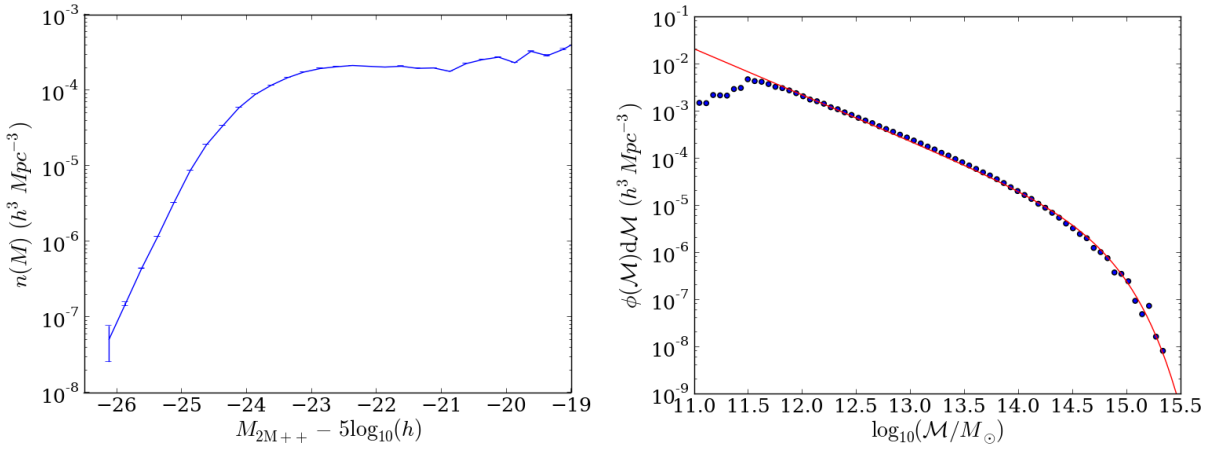

Figure B.1: Plotted on the left is the observed number density of galaxies within a magnitude bin of 0.25 Mag about an absolute magnitude indicated by the x-axis. Plotted on the right is the mass function derived from the Bolshoi halo catalogue. The solid red curve shown is the fit defined in Equation (B.3)

$$b_{\rm eff}^{\mathcal{M}}(r) = \frac{\int_{4\pi r^2 f_{\rm min}}^{\infty} b(L)\,\mathcal{M}(L)\,\Phi(L)\,dL}{\int_{4\pi r^2 f_{\rm min}}^{\infty} \mathcal{M}(L)\,\Phi(L)\,dL} = \psi^{\mathcal{M}}(r) b^*. \tag{B.4}$$

We compare this distance dependent mass weighted effective bias to its number and luminosity weighted counterparts in Figure B.3.

Secondly, before reconstruction of the mass weighted density field can be implemented, we must outline a new weighting scheme to account for incompleteness. We do so by first determining the mean mass of the objects not observed at a distance r, $\tilde{\mathcal{M}}$, as

$$\tilde{\mathcal{M}}(r) = \frac{\int_{L_{\rm min}}^{4\pi r^2 f_{\rm min}} \mathcal{M}(L)\,\Phi(L)\,dL}{\int_{L_{\rm min}}^{4\pi r^2 f_{\rm min}} \Phi(L)\,dL}, \tag{B.5}$$

where $L_{\rm min}$ is the minimum luminosity observable with 2M++. Using the reciprocal of the fraction of galaxies observed at r (*i.e.* the number weight $w^N(r)$ defined in Equation (2.2)), we in turn define the additive mass weight to be applied to galaxies at a distance r as

$$w^{\mathcal{M}}(r) = \tilde{\mathcal{M}}(r)[w^N(r) - 1]. \tag{B.6}$$

With the inclusion of these two alterations, the reconstruction procedure outlined in §2.5 can now be implemented.

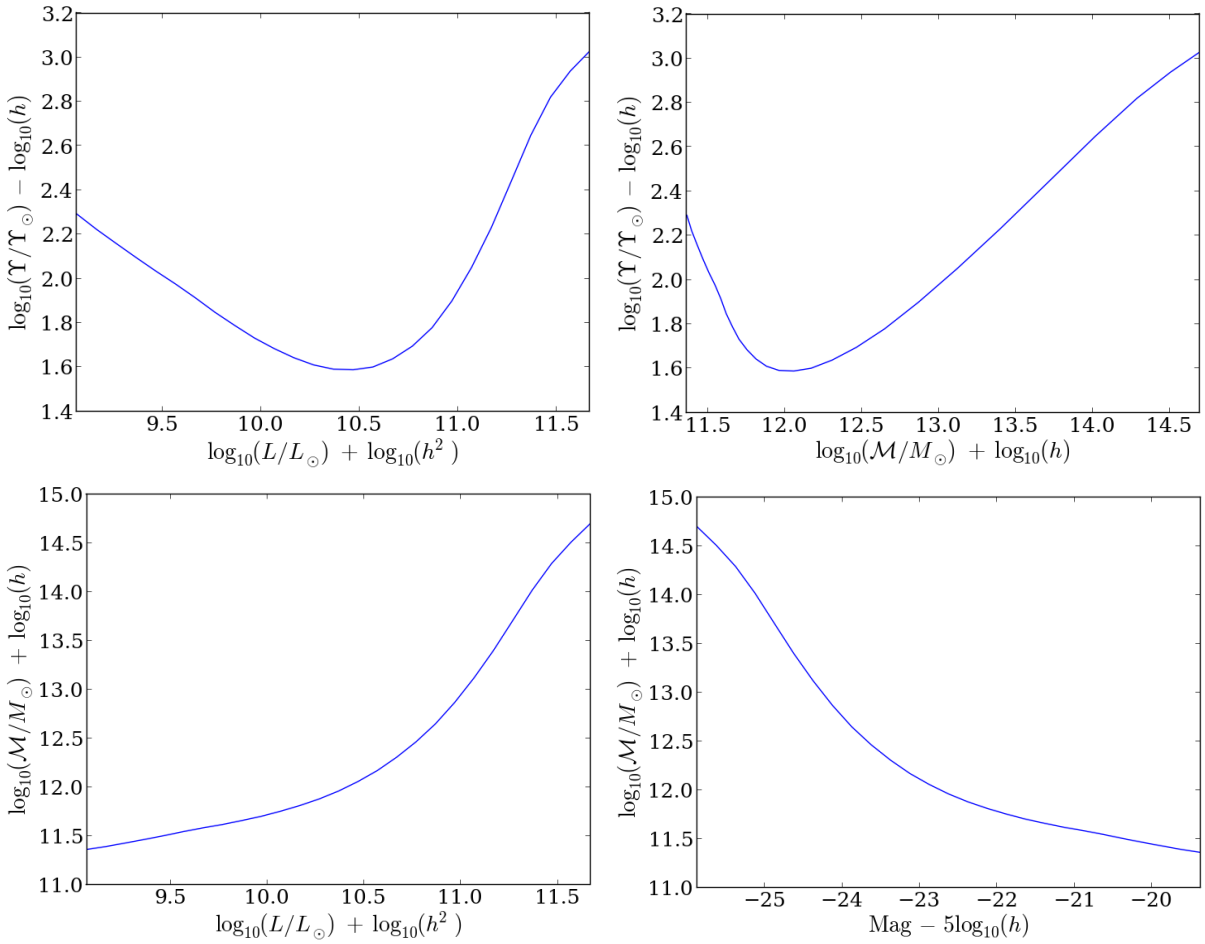

Figure B.2: Relations derived from an abundance matching scheme are shown above. The mass-to-light ratio as a function of luminosity and halo mass are shown in the two uppermost panels. In the lower panels halo mass as a function of luminosity and absolute magnitude are plotted.

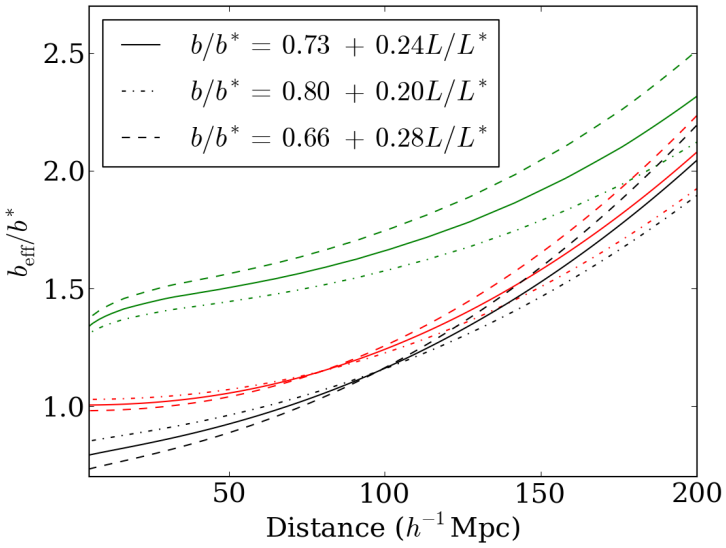

Figure B.3: Mass weighted effective bias as a function of distance for the most significant 1σ deviation of parameters from the scaling relation $b/b^* = (0.73 \pm 0.07) + (0.24 \pm 0.04)L/L^*$. The number weighted (black lower) and luminosity weighted (red central) effective biases are plotted for comparison.

B.3 Preliminary Results

We produced 100 density fields corresponding to $\beta^* = 0.01$ to $\beta^* = 1.00$ in steps of 0.01. For comparison, we plot the mass weighted density contrast of the supergalactic plane corresponding to $\beta^* = 0.43$ juxtaposed with the luminosity weighted SGP for the same value of β^* (Figure B.4). Surprisingly, the luminosity weighted field is found to be of higher overall contrast despite being comprised of fewer galaxies. Furthermore, there are several structures in the mass weighted case which are of considerably higher density contrast then the luminosity weighted case, *e.g.* (SGX, SGY) $\simeq$ (-100, 125) h^{-1}Mpc, and (50, -150) h^{-1}Mpc. The observed prominence of these structures likely arises from the large additive weights towards the periphery of the volume ($\sim 10^{14}$ $M_\odot$). The multiplicative weights at this depth ($\sim$10) are less susceptible to over weight noise.

When PV predictions derived from the mass weighted density field are compared to all measured velocities from A1 and SFI++, a value of $\beta^* = 0.48 \pm 0.03$ is obtained from the forward likelihood analysis. This value is somewhat higher than the preferred value reported in Chapter 4. The χ^2 value obtained, however, is significantly larger ($\chi^2/D.O.F. = 2212/2899$) in comparison to that found from luminosity weighting (2194/2899). Furthermore, from analysis of 500 bootstrap samples of the density field it was found that the uncertainty on β^* arising from sample variance was 7% for a mass weighting scheme, while only 3% for luminosity weighting. The reason for the larger value in the case of mass weighting results from discarding satellites before applying abundance matching to ob-

tain a density field. Preliminary results from this analysis, therefore, do not indicate that implementation of the mass weighting scheme discussed here is superior to the status quo.

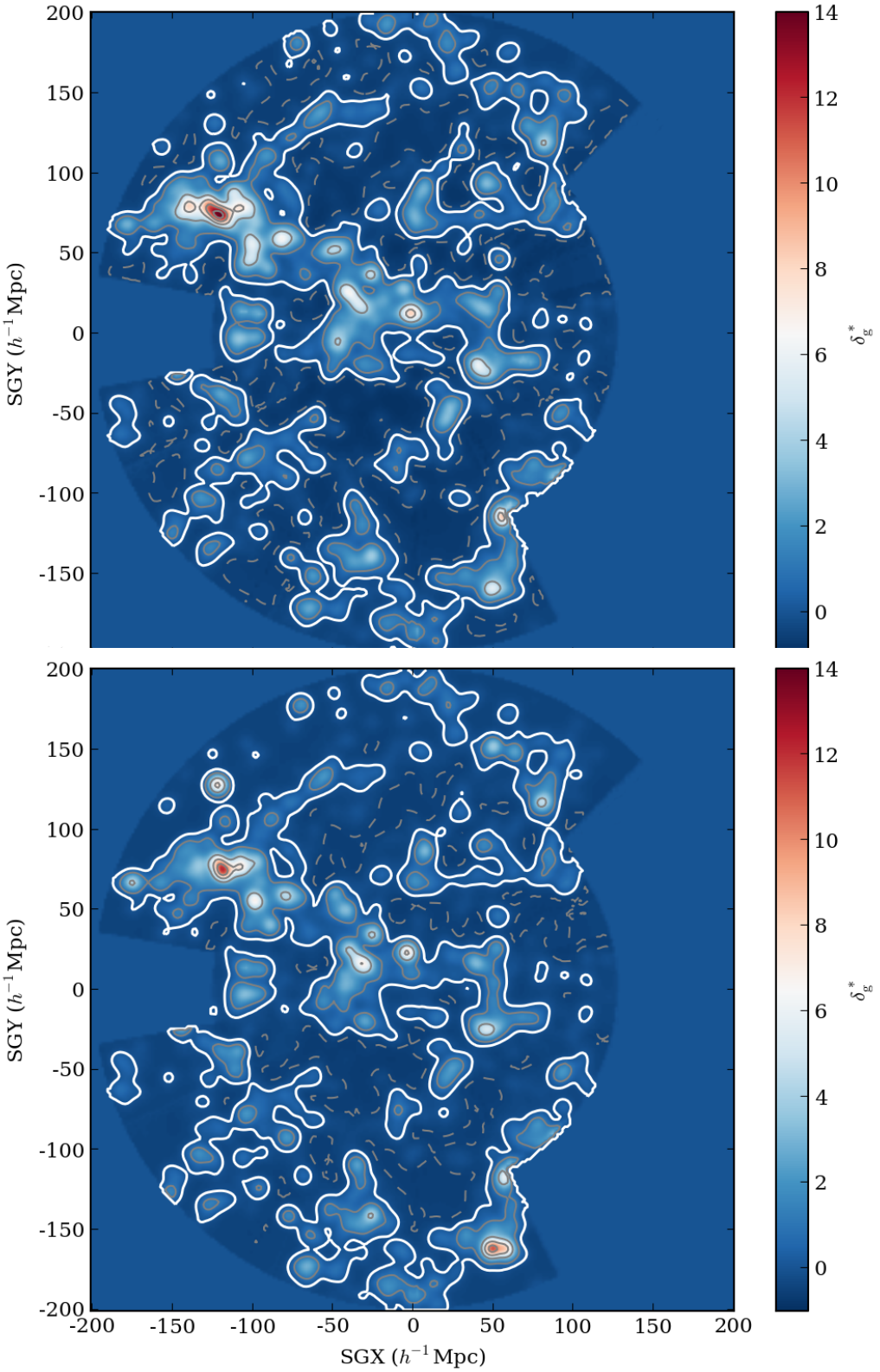

Figure B.4: Density contrast of the supergalactic plane corresponding to $\beta^* = 0.43$ obtained using a mass weighting scheme is shown directly above. The luminosity weighted SGP is shown in the uppermost panel for comparison.